

Southern Ocean Cloud Properties Derived from CAPRICORN and MARCUS Data

Gerald Mace¹, Alain Protat², Ruhi S Humphries³, Simon Peter Alexander⁴, Ian McRobert⁵, Jason Ward⁶, Paul Selleck³, and Melita D Keywood⁷

¹University of Utah

²Australian Bureau of Meteorology

³CSIRO

⁴Australian Antarctic Division

⁵Commonwealth Science and Industrial Research Organisation

⁶Commonwealth Scientific and Industrial Research Organisation

⁷Commonwealth Scientific and Industrial Research Organisation (CSIRO)

November 24, 2022

Abstract

The properties of Southern Ocean (SO) liquid phase non precipitating clouds (hereafter clouds) are examined using shipborne data collected during the Measurements of Aerosols, Radiation and Clouds over the Southern Ocean (MARCUS) and the Clouds Aerosols Precipitation Radiation and atmospheric Composition Over the SoutheRN ocean (CAPRICORN) I and II campaigns that took place in the Southern Ocean south of Australia during 2016 and late 2017 into early 2018. The cloud properties are derived using W-band radar, lidar, and microwave radiances using an optimal estimation algorithm. The SO clouds tended to have larger liquid water paths (LWP, 115 ± 117 g m⁻²), smaller effective radii (8.7 ± 3 μm), and higher number concentrations (90 ± 107 cm⁻³), than typical values of eastern ocean basin stratocumulus. The clouds demonstrated a tendency for the LWP to increase with presumably due to precipitation suppression up to of approximately 100 cm when mean LWP decreased with increasing . Due to higher optical depth, cloud albedos were less susceptible to changes in compared to subtropical stratocumulus. The high latitude clouds observed along and near the Antarctic coast presented a distinctly bimodal character. One mode had the properties of marine clouds further north. The other mode occurred in an aerosol environment characterized by high cloud condensation nuclei concentrations and elevated sulfate aerosol without any obvious continental aerosol markers that had much higher , smaller and overall higher LWP suggesting distinct sensitivity of the clouds to seasonal biogenic aerosol production in the high latitude regions.

1 Southern Ocean Cloud Properties Derived from CAPRICORN and MARCUS Data

2

3 Gerald G. Mace¹, Alain Protat^{2,5}, Ruhi S. Humphries^{3,5}, Simon P. Alexander^{4,5}, Ian M. McRobert⁶,
4 Jason Ward⁷, Paul Selleck³, Melita Keywood³

5

6 1. Department of Atmospheric Sciences, University of Utah

7 2. Australian Bureau of Meteorology, Melbourne, Australia

8 3. Climate Science Centre, CSIRO Oceans and Atmosphere, Aspendale, Australia

9 4. Australian Antarctic Division, Kingston, Tasmania, Australia

10 5. Australian Antarctic Programme Partnership, Institute for Marine and Antarctic Studies,
11 University of Tasmania, Hobart, Australia

12 6. Engineering and Technology Program, CSIRO Oceans and Atmosphere, Hobart, Australia

13 7. Climate Science Center/Atmospheric Composition and Chemistry/Aerosols, Oceans and
14 Atmosphere, CSIRO

15

16

17

18 Submitted to Journal of Geophysical Research, June, 2020

19

20

21

22

23

24 Corresponding Author Information:

25 Gerald "Jay" Mace, Professor

26 Department of Atmospheric Sciences, University of Utah

27 135 South 1460 East Rm 819 (819 WBB)

28 Salt Lake City, Utah, 84112-0110

29 Cell Phone: 801 201 7944

30 Office Phone: 801 585 9489

31 Email: jay.mace@utah.edu

32 Fax: 801 860 0381

33

34

35 Abstract: The properties of Southern Ocean (SO) liquid phase non precipitating clouds
36 (hereafter clouds) are examined using shipborne data collected during the Measurements of
37 Aerosols, Radiation and Clouds over the Southern Ocean (MARCUS) and the Clouds Aerosols
38 Precipitation Radiation and atmospheric Composition Over the SoutheRN ocean (CAPRICORN) I
39 and II campaigns that took place in the Southern Ocean south of Australia during 2016 and late
40 2017 into early 2018. The cloud properties are derived using W-band radar, lidar, and
41 microwave radiances using an optimal estimation algorithm. The SO clouds tended to have
42 larger liquid water paths (LWP, $115 \pm 117 \text{ g m}^{-2}$), smaller effective radii (r_e , $8.7 \pm 3 \mu\text{m}$), and
43 higher number concentrations (N_d , $90 \pm 107 \text{ cm}^{-3}$), than typical values of eastern ocean basin
44 stratocumulus. The clouds demonstrated a tendency for the LWP to increase with N_d
45 presumably due to precipitation suppression up to N_d of approximately 100 cm^{-3} when mean
46 LWP decreased with increasing N_d . Due to higher optical depth, cloud albedos were less
47 susceptible to changes in N_d compared to subtropical stratocumulus. The high latitude clouds
48 observed along and near the Antarctic coast presented a distinctly bimodal character. One
49 mode had the properties of marine clouds further north. The other mode occurred in an
50 aerosol environment characterized by high cloud condensation nuclei concentrations and
51 elevated sulfate aerosol without any obvious continental aerosol markers that had much higher
52 N_d , smaller r_e and overall higher LWP suggesting distinct sensitivity of the clouds to seasonal
53 biogenic aerosol production in the high latitude regions.

54

55 1. Introduction

56

57 The clouds fields of the Southern Ocean have emerged as one of the lynchpins in our
58 understanding of the Earth’s climate system (Tan et al., 2016; Frey and Kay, 2017, Kay et al.,
59 2016; Gettelman et al., 2020). While the circumpolar storm tracks are well known for
60 strong frontal systems wrapping deep midlatitude cyclones, it is the accompanying fields of
61 low level clouds, based mostly in the marine boundary layer (MBL), that seem to be critical
62 to understanding the radiative energy balance of this region (Bodas-Salcedo et al., 2012,
63 2014, 2016; 2019). These low-level clouds evolve from cumuliform to stratiform from just
64 behind the cold fronts to the upstream ridge. Inspired by the findings of Trenberth and
65 Fasullo (2010) who showed that too much solar energy is absorbed at the surface, studies
66 have increasingly focused on the ubiquity of supercooled liquid water in SO supercooled
67 clouds where predictions too aggressively reduce cloud cover through ice phase
68 precipitation processes (Vergara-Temprado et al., 2018; Frey and Kay, 2017). Recent
69 modelling studies have mitigated this bias through various means and have thereby shown
70 the sensitivity of the climate system to these SO MBL clouds (Tan et al., 2016; Kay et al.,
71 2016). Recent work (Mace et al., 2020; Mace and Protat, 2018a; O’Shea et al., 2017),
72 however, is suggesting that more mixed phase clouds are found in the Southern Ocean than
73 diagnosed from earlier spaceborne lidar data (Hu et al., 2009) even though the
74 concentrations of Ice Nucleating Particles are found to be extremely low (McCluskey, et al.,
75 2018).

76 How the properties of liquid phase clouds – especially supercooled liquid phase clouds –
77 vary across the SO remains an important topic. While the meteorology of the SO is
78 predictable, variations in factors that control the local and regional aerosol properties vary
79 considerably from regions north of the Antarctic Circumpolar Current (ACC) to the marginal
80 seas along the Antarctic (Armour et al., 2016; Fossum et al., 2018). While seasonally varying
81 sea surface temperatures and sea ice contribute to the cloud variability (Huang et al., 2016),
82 the Antarctic Circumpolar Current essentially divides the SO into lower latitude temperate
83 and high latitude marginal seas. Especially in the high latitude SO, seasonal biological
84 productivity results in significant seasonal oscillations in sulfate aerosol sources (Shaw,
85 1988; O’Dowd et al., 1997; Humphries et al., 2016; Ayers and Gras, 1991) that appear to
86 drive variability in cloud properties across the entire oceanic basin between winter and
87 summer (McCoy et al., 2015; Mace and Avey, 2017). Liquid clouds existing within this highly
88 variable environment respond both to the large-scale meteorological forcing and moisture
89 transports (McCoy et al. 2019; Klein et al., 2017; Kelleher and Grise, 2019) and to the local
90 aerosol environment. The large-scale environment provides the thermodynamic conditions
91 for producing clouds while the latter controls the detailed processes that determine when
92 and how low-level clouds precipitate (Savic-Jovcic and Stevens, 2008) and influence the
93 local surface energy budget (Protat et al., 2017).

94 In this study, we examine a particular genre of MBL clouds that form a significant
95 component of the total cloud population of the SO. Table 1 illustrates that geometrically
96 thin and non-precipitating MBL clouds feature prominently within the larger context of the
97 SO cloud climatology. We find that the SO, defined here as the circumpolar latitude belt
98 from 45 S to 70 S, has an overall cloud fraction of 86%. Of this overall cloud cover, 63% are

99 single layer. The MBL-based clouds can be roughly divided into two classes. Clouds with
 100 geometric thicknesses in excess of 1 km tend to be mostly precipitating (as defined by
 101 CloudSat) while roughly half of the MBL clouds have geometric thicknesses less than 1 km
 102 and exist as non-precipitating liquid phase layers. Because the non-precipitating thin clouds
 103 have radar reflectivities inconsistent with precipitation, or often exist within 1 km of the
 104 surface, they are largely unobserved by CloudSat (Marchand et al., 2008; Alexander and
 105 Protat, 2018) and, therefore, their properties are not well known.

106 Our objective in this study is to examine the microphysical properties of the non-
 107 precipitating clouds and quantify how they vary latitudinally within the Southern Ocean
 108 sector bounded by the East Antarctic coastline to Hobart (43S) and from 60E to 160 E using
 109 ship-based remote sensors from voyages by Australian Research Vessels between 2016 and
 110 2018. In particular, we examine dependencies between cloud droplet number (Nd),
 111 effective radius (re), and liquid water path (LWP) with various factors over the space and
 112 time covered by the observations. We consider how these clouds influence the surface
 113 solar radiation and the Top Of Atmosphere (TOA) albedo. We also consider how the cloud
 114 properties are associated with well-defined aerosol regimes characterized during the
 115 campaigns.

116
 117 Table 1: Vertical occurrence data from CloudSat (Stephens et al., 2008) and CALIPSO
 118 (Winker et al., 2009) between 2007-2010 using the combined characterization of Mace and
 119 Zhang, (2014) in the 40s-70s latitude belt.

Total Cloud Columns Meeting MBL, Single Layer Conditions: 17,399,960			
	0-1 km	1-3	3-5
Total	0.47	0.48	0.05
Precipitating	0.08	0.67	0.97

120
 121 2. Data and Methods
 122

123 In this study we use data from recent voyages by Australian vessels between Hobart, Tasmania
 124 and Antarctica (Figure 1). These voyages included a similar set of remote sensing
 125 measurements that allow us to apply an identical cloud property retrieval algorithm to each
 126 campaign data set. The critical measurements include radar reflectivity (dBZ_e) profiles from
 127 vertically pointing W-Band radars, attenuated backscatter (β_{obs}) profiles from vertically
 128 pointing optical lidars, downwelling microwave brightness temperatures T_b at 31 GHz from
 129 Radiometric radiometers, and regular radiosonde soundings. Surface meteorological
 130 measurements, sea surface temperatures, and downwelling solar and infrared broadband
 131 fluxes were also collected in each campaign. Extensive aerosol measurements were also made
 132 during these campaigns. Of relevance to the present study are the cloud condensation nuclei
 133 (CCN) and sulfate aerosol observations.

134 The first of these voyages took place aboard the Australian Research Vessel (RV)
 135 *Investigator* in March and April of 2016 (Mace and Protat, 2018a and b, hereafter MP18a and
 136 MP18b, respectively). Unlike the other voyages, the 2016 voyage, hereafter referred to as
 137 CAPRICORN I spent its nearly 5-week duration north of 53°S and most that time near 45°S and

138 142°E servicing Southern Ocean Time Series buoys (Schulz et al., 2012). In total we use 137
139 hours of non-precipitating liquid cloud data from CAPRICORN I.

140 CAPRICORN II was an observational campaign also conducted on board the Australian
141 Research Vessel (RV) *Investigator* during a voyage from Hobart to the Antarctic Shelf between
142 January 11, and February 21, 2018. CAPRICORN II occurred in conjunction with the U.S.
143 National Science Foundation-sponsored Southern Ocean Cloud Radiation Aerosol Transport
144 Experimental Study (SOCRATES) campaign (McFarquhar et al., 2020). SOCRATES featured 15
145 flights by the National Center for Atmospheric Research (NCAR) Gulfstream V. CAPRICORN II
146 included the same cloud instruments that participated in CAPRICORN I as described in MP18a.
147 In this study we focus on data from the W-Band Doppler Cloud radar, 355 nm Lidar, and a two-
148 channel microwave radiometer with the addition of a radar wind profiler, from the NCAR
149 integrated sounding system. During the 7-week voyage, approximately 300 radiosondes were
150 launched on a 3-6 hourly schedule depending upon weather.

151 The CAPRICORN II voyage track was mostly determined by oceanographic objectives
152 that included some 88 preplanned stations at which conductivity, temperature, depth (CTD)
153 and trace metal soundings of the water column were conducted. Stations were occupied along
154 the 130° to 150° E meridians during the voyage with a delay at each station for 6-24 hours
155 depending on oceanographic objectives. Stations were separated by an average of
156 approximately 50 km. From an atmospheric sampling perspective, small steps with roughly
157 half-day delays allowed for a unique characterization of the structure of cloud and
158 thermodynamic properties of the Southern Ocean summer atmosphere. *Investigator* passed
159 south of 50°S on 18 January and 60°S on 27 January both along the 140°E meridian. The
160 southernmost point was reached on February 2 near the seasonal ice edge at 66°S. *Investigator*
161 then remained south of 60°S occupying stations between 132 and 150 E until 15 February.
162 Following the final oceanographic station occupied near 57° S and 132° E on 16 February
163 *Investigator* made a brief eastward excursion to coordinate with a GV flight on 18 February
164 near 57°S 140°E and another minor diversion to coordinate with a descending overpass of the
165 CALIPSO satellite at 48°S and 144°E on 20 February. We use 78 hours of non-precipitating MBL
166 clouds from CAPRICORN II.

167 The MARCUS campaign featured components of the U.S. Department of Energy's (DOE)
168 Atmospheric Radiation Measurement (ARM) program's second Mobile Facility (AMF2) deployed
169 on board the Australian ice breaker RSV *Aurora Australis* during the 2017-2018 Antarctic
170 summer resupply voyages. Based out of Hobart, four voyages took place from early November,
171 2017 through March, 2018 (Figure 1). The key instrumentation that we use are β_{obs} from a
172 Micropulse Lidar, Tb from a Radiometrics microwave radiometer (Liljegren, 1994; Liljegren et al.
173 2001), and radar reflectivity profiles from the Marine W-Band ARM Cloud Radar (M-WACR).
174 Radiosondes were launched on a 6-hourly schedule when away from Hobart and these were
175 supplemented by the standard ship-based meteorological and sea surface temperature
176 measurements. Unlike the CAPRICORN voyages, the purpose of the four *Aurora Australis*
177 voyages were to resupply the Australian Antarctic stations. Therefore, the ship steamed from
178 Hobart to and from the Antarctic coast directly, while avoiding bad weather and as much of the
179 early-season thick sea ice as possible. Each 1-way transit to and from Antarctica took from 7 to
180 10 days depending on destination. The ship's speed reduced in sea ice and the ship spent up to
181 two weeks at each station for the resupply operations. The final voyage of the season to and

182 from Macquarie Island (55°S) occurred during the first two weeks of March. Most instruments
183 were not operated while the ship was moored in Hobart between voyages. In total, we use 265
184 hours of non-precipitating cloud data from Marcus.

185

186 3. Method

187

188 We seek to examine the properties of an important genre of clouds that influence the
189 radiative properties and cloud optical depth feedbacks in the Southern Ocean. Non-
190 precipitating liquid clouds are ubiquitous across the Southern Ocean and compose roughly half
191 of all clouds in the MBL (Table 1). From an analysis standpoint, the single-phase liquid and non-
192 precipitating clouds require a minimum of assumptions in developing algorithms needed to
193 infer their properties, thereby minimizing uncertainty. We implement an optimal estimation
194 algorithm that derives the layer mean liquid water path (LWP), the layer mean effective radius
195 (r_e) and the cloud droplet number concentration (N_d) using an optimal estimation (OE)
196 algorithm that combines β_{obs} , dBZe, and Tb. Reasoning that β_{obs} constrains approximately the
197 2nd moment of the droplet size distribution (DSD), dBZe constrains the 6th moment of the DSD
198 in the Rayleigh scattering regime, and Tb provides an integral constraint on the vertically
199 integrated condensed water (LWP), the measurement combination uniquely constrains the
200 DSD. Note that in CAPRICORN II and MARCUS, the W-Band radars were on stabilized platforms.
201 This was not the case in CAPRICORN I. Therefore, we do not use the Doppler velocity in this
202 study which would be an interesting addition in this cloud genre to constrain vertical motions
203 and turbulence. Our retrieval methodology is based on the approach described in Mace and
204 Protat (2018b). However, we will describe the algorithm in detail because of several
205 improvements made since that initial study. Our basic assumptions, however, are largely
206 unchanged.

207 To illustrate our methodology (Figure 2), we use a time section of measurements from
208 CAPRICORN II collected on January 29 when the ship was in the vicinity of 64°S and 140°E. This
209 day was characterized by an overcast MBL cloud layer that precipitated until late in the day.
210 There were 8 soundings launched during this 24 hour period.

211

212 3.1 Initial Data Processing and Calibration

213

214 The lidar measurements that we use were collected from a 532 nm Micropulse Lidar for
215 MARCUS and from a 355 nm RMAN lidar system in CAPRICORN I and II (See Royer et al. 2014
216 and MP18a for a brief description of the RMAN system). Both systems provide an elastic
217 backscatter and depolarization channel. While the RMAN system does provide a Raman
218 scattering channel, the sensitivity of the system is such that long integration times in cloud-free
219 tropospheric air are required for calibration (Alexander and Protat, 2019). In our earlier work
220 (MP18b) we relaxed the β_{obs} profile to theoretical Rayleigh β_{obs} profiles from clear sky nights.
221 The calibration of the lidar, however, drifts significantly on timescales of hours resulting in large
222 uncertainties in β_{obs} that we accounted for in our earlier work by increasing the error in β_{obs} in
223 the OE algorithm. Here, we implement a calibration method that is particularly suitable for the
224 clouds that we are considering using a methodology described first by O'Connor et al. (2004).

225 From the early work of Platt et al. (1999) and following Li et al., (2011), we express the
 226 observed attenuated backscatter as

$$227 \quad \beta_{obs}(z) = \beta(z)e^{-2 \int \sigma dz} \quad (1)$$

228 Where the measured β_{obs} is the result of 2-way attenuation through the cloud to a point z in
 229 the layer and σ is the extinction coefficient with units of inverse length where σ is expressed in
 230 terms of the lidar ratio, $S = \frac{\sigma}{\beta}$, and a factor η that accounts for the addition of photons to the
 231 observed signal due to multiple scattering in optically dense clouds allowing use to write (1)

$$232 \quad \beta_{obs}(z) = \beta(z)e^{-2\eta Sr} \quad (2)$$

234 Where we are averaging over the layer through a range r . Defining the layer-integrated total
 235 attenuated backscatter as $\gamma = \int \beta_{||+\perp}$ and the layer integrated depolarization ratio as $\delta = \frac{\int \beta_{\perp}}{\int \beta_{||+\perp}}$

236 we can express $\eta = \left(\frac{1-\delta}{1+\delta}\right)^2$ (Hu et al. 2006a,b). Platt et al. (1999) relates S with η according to
 237 $S\eta = \frac{1-T^2}{2\gamma}$ and where T is the layer transmittance. When the layer is fully attenuating ($T=0$) and

$$238 \quad S = \frac{1}{2\eta\gamma} \quad (3).$$

239 O'Connor et al. (2004) and Hu et al. (2009) among others show that S varies over a
 240 narrow range in liquid water clouds with an average near 18.8. We confirmed this by
 241 examining S calculated from Mie theory using observed DSDs collected in water clouds during
 242 Rain in Clouds over the Ocean (RICO; Rauber et al., 2006). We found that S and r_e vary
 243 systematically (Mace et al. 2020), with a small dynamic range of S from 17-19 for >90% of all
 244 cloud DSDs observed during RICO. This range is small with respect to the calibration
 245 uncertainty in measured β_{obs} for elastic lidars and in the assumptions used to derive Equation
 246 3. Following O'Connor et al. (2004) therefore, we assume that S in water clouds can be fixed at
 247 a mean value of 18.7 (the mean value we found from the RICO DSDs) that corresponds to an
 248 assumed r_e of ~ 10 μm . We effectively calibrate the lidar signal by adjusting γ by a factor that
 249 gives $S=18.7$ on a profile-by-profile basis. This method of auto-calibration (O'Connor et al.'s
 250 term) then allows us to have a physically consistent characterization of β_{obs} independent of
 251 using the Rayleigh method in nighttime cloud-free skies. Application of this method to the data
 252 collected on January 29 is shown in Figure 2 where a mean factor of 3.5 is applied to the
 253 observed lidar β_{obs} on this day to achieve an S of 18.7. The limitations of this method are
 254 obvious since we implicitly make an assumption that the layer-mean effective radius is
 255 approximately 10 μm . However, as we show below, the OE inversion methodology allows the
 256 final solutions to depart from this assumption.

257 As the lidar signal penetrates into an optically thick cloud, β_{obs} becomes increasingly
 258 dominated by multiply scattered light becoming increasingly depolarized relative to the
 259 transmitted signal and this effect is quantified by η . The 355 nm system will have a sharper
 260 forward diffraction peak than the 532 nm MPL system, resulting in less integrated backscatter
 261 and lower values of η . This weaker signal is compensated by the lower background signal in the
 262 UV channel compared to the MPL. Typically, β_{obs} increases from cloud base to a maximum
 263 value a few range bins into the layer, and β_{obs} then begins an exponential decay as it becomes
 264 increasingly dominated by multiply-scattered light. Following Li et al. (2011), If we take the

265 natural logarithm of both sides of equation 1, we can write $\eta\sigma = -\frac{\ln\beta_{obs}-\ln\beta}{2r}$ where the right
266 hand side is the logarithmic decay of the multiply-scattered signal with depth. Because we
267 have estimated η from measurements (independent of calibration), we can make a
268 determination of σ in the optically thick part of the layer beyond the peak in β_{obs} . Li et al.
269 (2011) compare σ derived from this method to estimates of σ derived from passive reflectance
270 techniques and find an uncertainty of $\sim 13\%$. The accuracy of this method is dependent on
271 calculating the rate at which the signal decays with depth in the layer. In practice, we fit a
272 regression line to β_{obs} at heights above the layer maximum in β_{obs} until the signal is a factor of
273 2 above the noise floor that is determined from the mean β_{obs} well above the fully attenuating
274 cloud layer. The goodness of the linear regression fit depends on the number of measurements
275 in this range and the accuracy is dependent on the vertical resolution of the lidar
276 measurements when σ is large. The vertical resolution of the RMAN and MPL data during these
277 campaigns is 15 m. We find that for clouds with σ less than 50 km^{-1} we are able to use 3-5 data
278 points to estimate the slope. When σ becomes much larger than 75 km^{-1} , we find that typically
279 only 2-3 points are available and the uncertainty in σ becomes large. We found this to be a
280 limiting issue in only a few cases near the coast of Tasmania when the clouds existed within
281 continental air masses. Figure 2 shows lidar data from a case collected on January 29. We find
282 that on average the layer observed on January 29 had a mean σ of approximately 20 km^{-1}
283 varying from 10 to 40 km^{-1} . This case is discussed in more detail below.

284 To separate liquid phase clouds from clouds that are mixed phase, we follow the
285 approach used in MP18A where we examine the sub cloud for measurable signal
286 depolarization. In warm clouds for CAPRICORN I and II and MARCUS after 15 January where
287 precipitation is known to be liquid, we found that the vertically resolved sub cloud
288 depolarization ratios were reliably less than 0.1 and in situations when the precipitation was
289 known to be frozen, the sub cloud depolarization ratios typically exceeded 0.2. Figure 2 shows a
290 time series of sub cloud depolarization ratios from a cloud layer with base temperature near -
291 8°C that was producing occasional frozen precipitation at the surface noted by observers. We
292 see pockets of ice phase precipitation from this layer but most of the precipitation observed by
293 the radar was liquid and did not reach the surface. A known issue exists with the MARCUS MPL
294 during the first half of the campaign (through voyage 2 that ended on 12 January) where the
295 window through which the MPL viewed the atmosphere changed the polarization state of the
296 laser light. This resulted in the minimum depolarization ratio measured by the instrument to be
297 ~ 0.2 . This issue was corrected in Hobart on 15 January 2018 prior to voyage 3. Since we found
298 that when ice was present near cloud base, the depolarization ratios typically exceeded 0.4, we
299 use a threshold of 0.3 for the early MARCUS voyages to identify the presence of ice while for
300 later MARCUS and CAPRICORN I and II, we use a sub cloud depolarization ratio of 0.25 as a
301 threshold.

302 The vertically pointing millimeter radars used in CAPRICORN I and II and MARCUS were
303 W-Band Doppler systems. In CAPRICORN I and II the radars used were the Bistatic Radar
304 System for Atmospheric Studies (BASTA; Delanoë et al., 2016). The BASTA radar observations
305 were calibrated using statistical comparisons between BASTA, the Ku-band micro rain radar,
306 and Ku-band and W-band T-matrix calculations using the ODM470 disdrometer observations
307 from the mast (see Klepp et al. 2018 for more details and CAPRICORN I results). BASTA cloud

308 radar observations from ground-based deployments surrounding the CAPRICORN experiments
 309 were also compared statistically with CloudSat reflectivities using the technique outlined in
 310 Protat et al. (2011), confirming the calibration figures derived from the disdrometer and micro
 311 rain radar comparisons (not shown).

312 As noted recently by Kollias et al., (2019), the ARM millimeter radars are subject to
 313 significant calibration uncertainties. Specifically, Kollias et al, (2019) compared the M-WACR
 314 measurements with CloudSat and noted that the M-WACR calibration ranges from 4 to 8 dB
 315 lower than the well-calibrated W-Band radar on CloudSat (Tanelli et al., 2008). Such a
 316 calibration uncertainty is prohibitive for quantitative use of the radar reflectivities, and no
 317 direct means of calibrating the M-WACR system were available during MARCUS. Furthermore,
 318 during late 2017 and early 2018, CloudSat was involved in a transition in orbit so regular data
 319 were not collected. In order to establish some means of assessing the calibration of the M-
 320 WACR, we reason that the RSV Aurora Australis and the RV Investigator were collecting data in
 321 a similar region during a common period of time and aspects of their data should, therefore, be
 322 similar. In particular, with both BASTA and M-WACR operating near 94 GHz, we would expect
 323 that the radar reflectivity statistics of the sub-cloud base liquid precipitation observed during
 324 their common sea time (January and February) and common latitude range (north of 66S)
 325 should be similar. We therefore examine the radar reflectivity statistics in the 200 m above the
 326 radars and up to 1 range bin below the lidar cloud base (to a maximum height of 1 km) when
 327 the lidar depolarization ratios below a measured cloud base indicated the presence of liquid
 328 hydrometeors and the BASTA dBZe recorded values in excess of -20 dBZe. The results are
 329 shown in Figure 3. We find that the M-WACR is indeed offset low from the results measured by
 330 the calibrated BASTA radar during CAPRICORN II. Adding 4.5 dB to the M-WACR sub-cloud
 331 precipitation results causes the two histograms to come into alignment (Figure 3 shows the
 332 uncorrected MARCUS results). This offset is consistent with the findings of Kollias et al (2019)
 333 and therefore, in all results presented henceforth this offset will be added to the M-WACR dBZe
 334 measurements.

335

336 3.2 Algorithm to Derive N_d , LWP, and r_e

337

338 The non-precipitating liquid phase clouds that we examine are assumed to be composed
 339 of a single mode of droplets that can be described by a modified gamma distribution,

$$340 \quad N(D) = N_0 \left(\frac{D}{D_0}\right)^\alpha \exp\left(-\frac{D}{D_0}\right) \quad (3)$$

341 Where $N(D)$ is the droplet number per unit size and has units of cm^{-4} . N_0 , D_0 , and α are
 342 characteristic number, diameter and the shape parameter of the DSD. All units are cgs unless
 343 specified otherwise. This simple integrable function allows us to express the microphysical
 344 quantities, N_d (cloud droplet number), q (liquid water content), and r_e (effective radius) with the
 345 following expressions,

346

$$N_d = N_0 D_0 \Gamma(\alpha + 1)$$

347

$$q = \rho \frac{\pi}{6} N_0 D_0^4 \Gamma(\alpha + 4) \quad (4)$$

348

$$r_e = \frac{D_0}{2} (\alpha + 3)$$

349 Where we have used the recursion properties of the gamma function in the ratio of the third
 350 and second moments of $N(D)$ for r_e . See Posselt and Mace (2014, their appendix B). Similarly,
 351 we can relate observable quantities to $N(D)$ using the appropriate moments. The radar
 352 reflectivity parameter, Z_e , can be written as the sixth moment of $N(D)$

$$353 \quad Z_e = 10^{12} N_0 D_0^7 \Gamma(\alpha + 7) = 10^{12} \frac{48}{\pi} r_e^3 q F_6. \quad (5)$$

354 Where the constant 10^{12} converts from cgs to the typical units for Z_e of $\text{mm}^6 \text{m}^{-3}$ and $F_6 =$
 355 $\frac{(\alpha+6)(\alpha+5)(\alpha+4)}{(\alpha+3)^3}$ arises from the recursion properties of the gamma function. Equation 5

356 assumes that the droplets remain small with respect to the wavelength of the radars ($\sim 3\text{mm}$) so
 357 that the Rayleigh approximation is valid. The lidar backscatter and extinction coefficients are
 358 similarly derived from second moments of $N(D)$ times $\frac{\pi}{4}$ multiplied by the extinction efficiency
 359 (here assumed to be 2) and the backscatter efficiency which is assumed constant at 0.12
 360 (MP18b), respectively (see Posselt and Mace, 2014).

361 The OE inversion methodology is convenient for arriving at solutions to problems using
 362 disparate data streams that account for uncertainties in observations and assumptions given
 363 prior statistics (Maahn et al., 2020; Mace et al., 2016). The method we use is adapted from
 364 Rogers et al (2000) and minimizes a cost function using Gaussian statistics and Newtonian
 365 iteration. In a problem with several degrees of freedom and inherent uncertainties in
 366 observations and forward models, it is often necessary to begin the iteration with a physically
 367 reasonable first guess to avoid converging on an unphysical local minimum of the cost function
 368 generated by uncertainties. To arrive at this first guess, we combine Z_e , σ derived from β_{obs}
 369 and T_b . We use a simplified analytical model relating T_b and LWP (MP18b),

$$370 \quad \delta T_b = T_{eff} \left(1 - \exp \left(-\frac{3}{2} a_b LWP \right) \right) \quad (6)$$

371 Where δT_b is the increase in 31 GHz T_b caused by the presence of the cloud layer and $a_b =$
 372 1.712 is the mass absorption coefficient in cgs units (MP18b). The measurements then
 373 constrain the mass and the cross-sectional area of what we assume to be a layer-mean DSD.
 374 We then iterate to estimate α using Z_e as a constraint. Reasonably often, however, the W-Band
 375 radars do not detect the non-precipitating cloud layers. This occurs approximately 25% of the
 376 time for CAPRICORN I and II and 15% of the time during MARCUS (we estimate the M-WACR
 377 was ~ 5 dB more sensitive than the BASTA radars). In such cases we fix our initial estimate of α
 378 at a mean value of 2.5 derived from in situ data collected during SOCRATES. This first guess
 379 $N(D)$ is then used to begin the OE iteration.

380 The OE algorithm that we employ is identical to that described in MP18b starting at
 381 equation 12 of that paper with all observations interpolated to the time indexes of the BASTA
 382 radar. The main difference between the earlier work and here is that the β_{obs} measurements
 383 are calibrated using the method described earlier and the first guess is constrained by the
 384 extinction coefficient derived from the lidar data. Because we start with a microphysical
 385 estimate that already reasonably replicates the measurements, the final solution does not
 386 depart substantially from the first guess. Therefore, the constraints provided by the lidar-
 387 derived extinction are a critical new feature of this updated approach. Another important
 388 difference between MP18b and this analysis is that we use prior statistics derived from the in-
 389 situ data collected during SOCRATES (Wang et al., 2020). Therefore, the algorithm produces
 390 results that are statistically similar to this specific prior knowledge of SO clouds. We also focus

391 on N_d in this study. While we do not retrieve N_d specifically, we derive it from the retrieved
392 LWP, r_e , and α . We use the uncertainties of the retrieved quantities with a bootstrap approach
393 (Kirk and Stumpf, 2009) to estimate the uncertainty in N_d . This is discussed in more detail
394 below where we explain and demonstrate uncertainty and validation of the algorithm. We also
395 use solar flux radiative closure as a means of validation. This is discussed in more detail in the
396 following sections.

397 398 4. Results

399 400 4.1 January 29 CAPRICORN II Case Study

401
402 During the latter of half the UTC day on 29 January 2018 the R/V Investigator was stationary
403 near 63.5°S and 139.8°E in the cold sector of a deep cyclone that had passed early during the
404 UTC day on 28 January. On 29 January the low pressure was centered near 65°S and 170°E. At
405 the R/V Investigator location, surface temperatures were just below freezing during much of
406 the day on 29 January and occasional light snow grains were reported from an overcast
407 stratocumulus layer by radiosonde operators during 3-hourly launches. Winds were sustained
408 southerly around 20 knots and surface pressures rose steadily from a minimum of 965 mb early
409 on 28 January to 985 mb at 18 UTC to 990 mb by 00 UTC on 30 January. Figure 2a and b show
410 that at 15 UTC on 29 January the cloud layer base was near 750 m and the radar layer tops
411 extended to ~1.5 km. The BASTA w-Band radar observed occasional light precipitation from
412 this overcast layer and Lidar depolarization ratios suggest that the sub cloud precipitation was
413 mostly liquid with pockets of ice phase typically associated with peaks in the radar reflectivities
414 but not always. The MRR recorded light precipitation during several brief periods (less than a
415 few minutes in duration) prior to 12 UTC on 29 January but none after 12 UTC and no
416 precipitation was recorded by the ship rain gauge suggesting that the precipitation was very
417 light. The sounding at 1600 UTC (not shown) indicates that the lifting condensation level (LCL)
418 was near cloud base at -8°C with a marine inversion base near 1.3 km at -14°C and inversion top
419 near 1.45 km. The 1600 UTC sounding indicates that the MBL was well mixed from the surface
420 to cloud base. After 1600 UTC, the light precipitation observed by the W-Band radar became
421 lighter and less frequent and after 18 UTC, the radar reflectivity of the layer fell below the
422 detection threshold of the W-Band although the cloud layer was persistent through 21 UTC
423 according to the lidar and microwave radiometer. Lidar-derived extinctions in this layer were
424 steady between 30 and 40 km⁻¹. This layer was well characterized by the RMAN lidar with
425 uncertainties in the extinction in the range of 20-30%.

426 As the precipitation mostly ceased after 16 UTC, we are able to derive cloud properties
427 from the remote sensing data in the supercooled liquid cloud layer using the method described
428 above. In the hour between 16 and 17 UTC, water paths were steady between 200 and 300 g
429 m⁻² (Fig. 2e) with uncertainties near 15%, effective radii were variable but averaged 12 μm (Fig.
430 2f) with uncertainties in the 10% range and N_d was mostly below 50 cm⁻³ (Fig. 2g) with
431 uncertainties of approximately 70-80%. As the precipitation ceased and the radar reflectivity
432 decreased to below the detection threshold of the BASTA w-band, the water path of the layer
433 gradually decreased and became variable (Fig. 2e). Note that as the reflectivity dropped below
434 the BASTA detection threshold, the uncertainty of r_e and N_d increases. This is the result of how

435 we handle the OE inversion when the radar is unable to sense the layer. Because we know the
436 radar detection threshold, we know that the maximum radar reflectivity in the layer must be
437 lower than that threshold. Therefore, we set the radar reflectivity to -35 dBZe and assume that
438 the uncertainty in that reflectivity is 5 dB. This allows us to use the measurements of LWP and
439 σ and use the knowledge that the dBZe is lower than the detection threshold. The
440 uncertainties in r_e , then increase to be typically on the order of 50% and the uncertainties in N_d
441 increase to $\sim 120\%$.

442 An interesting aspect of this case study is that before the layer became completely
443 undetectable by the w-band, r_e and N_d begin opposite trends with N_d increasing and r_e
444 decreasing. This change begins near 17:10 UTC and by 17:30 UTC r_e is steady near 8 μm while
445 N_d effectively doubles to be in the 100 cm^{-3} range. These changes then persist through the
446 remainder of the period even when the layer is observable by radar at a few instances. We
447 note this because we see an associated change in aerosol properties and chemical composition
448 recorded at the surface about an hour after the change in the cloud layer (Figure 2h). CCN at
449 0.55% super saturation increases from $\sim 150 \text{ cm}^{-3}$ to 300 cm^{-3} and the sulfate mass
450 concentration in submicron aerosol increases from 0.2 to $0.5 \mu\text{g}/\text{m}^3$ as measured by the Time
451 of Flight Aerosol Chemical Speciation Monitor (ToF-ACSM; Fröhlich et al, 2013).. The step
452 increases in aerosol properties are consistent with increased N_d and decreased r_e . We note that
453 LWP becomes variable and decreases but does not seem to be responding in a similar stepwise
454 fashion as do r_e and N_d . The lidar data and associated derived products do not demonstrate an
455 abrupt transition at this time. We do note that over the period shown in Figure 2 the cloud
456 base as derived from lidar β_{obs} lifted gradually and evidence for sub cloud precipitation became
457 more sparse. A careful examination of the δ and η also demonstrate a gradual increase and
458 decrease, respectively, between 11 and 20 UTC. This would be consistent with droplets
459 becoming smaller and N_d increasing although σ remains near 20 km^{-1} through the period.

460 The ~ 1 hour time offset in changes between the surface aerosol and cloud layer is
461 curious. Recall that the 16 UTC sounding showed the MBL to be well mixed. However, a
462 sounding launched at 19 UTC showed that the inversion base had descended to 1.2 km (top
463 remained near 1.4 km) and the surface layer was decoupled from the deeper MBL by a weak
464 inversion at 200 m. Below 200 m height, the humidity was largely unchanged while above 200
465 m the profile had dried considerably in the intervening three hours likely explaining the
466 decrease in LWP. It is plausible that free tropospheric air containing biogenic sulfate aerosol
467 had mixed into the MBL reducing humidity and influencing cloud properties. Because the MBL
468 was decoupled, it took some time for that change to be mixed to the surface.

469 We further note that this step change in aerosol chemistry and CCN is similar to events
470 described by Humphries et al. (2016) at similar latitudes and times of year. Up to this time
471 during CAPRICORN II, sulfate concentrations had remained mostly below $0.2 \mu\text{g m}^{-3}$ and the
472 step change on 29 January to values in excess of $0.4 \mu\text{g m}^{-3}$ marked the beginning of elevated
473 surface CCN and sulfate that persisted until 4 February while the ship operated south of 65 S.
474 Markers of continental air mass origin such as radon were absent during this period, however
475 this may not be expected if air masses originated from the ice-coved Antarctic continent. Cloud
476 droplet numbers during this time remained mostly elevated in excess of $\sim 100 \text{ cm}^{-3}$ until 4
477 February when extended poor weather precluded cloud retrievals until 15 February. See

478 McFarquhar et al. (2020) their figure 3 for a daily summary of CAPRICORN II cloud and aerosol
479 time series that illustrate these events.

480

481 4.2 Cloud Properties

482

483 One of the key motivating factors for the SO measurement campaigns is the surface
484 solar radiation bias common to many climate models. However, actual measurements of
485 surface solar radiation and associated clouds are rare in the SO. Here, we explore the
486 properties of a genre of clouds that are key components of the surface energy balance of this
487 region. We combine data from the MARCUS and CAPRICORN campaigns into a single data set
488 that brackets the Austral Summer months from November through mid-April and ranges in
489 latitude from the East Antarctic coast where the Aurora Australis spent several weeks of its
490 campaign to the latitude of Hobart near 42°S that was the common home port for both vessels.
491 In total, we consider 480 hours of retrieved cloud properties. We find that the non-precipitating
492 clouds in this region during the warm season are composed of layers with LWP in the range of
493 90 g m^{-2} with a standard deviation of about 100 g m^{-2} , r_e near $8.7 \mu\text{m} \pm 3 \mu\text{m}$, and N_d near 90
494 cm^{-3} with about a 200% standard deviation (Figure 4). In Figures 4b and 4c, we compare the
495 retrieved values with distributions derived from the SOCRATES in situ microphysical
496 measurements where we exclude the precipitation mode in bimodal liquid droplet distributions
497 (Mace et al., 2016). We have also compared q by dividing the retrieved LWP by the layer
498 thickness with the q measured in situ and found similarly unbiased agreement (not shown).
499 The offset that we see in the in situ and retrieved N_d distributions is expected because the
500 larger N_d values in the retrievals are derived from cases near Antarctica and also close to
501 Tasmania where SOCRATES did not sample (see McFarquhar et al., 2020 and below). We note
502 that the retrieved cloud properties are in broad agreement with similar quantities derived from
503 A-Train data (Mace and Avey, 2017; McCoy et al., 2015) where they demonstrate that the
504 microphysical properties of these clouds vary seasonally with higher N_d and lower r_e during
505 summer than winter associated with changes in aerosol derived from biogenic sources.
506 Because the A-Train is limited to layers above 1 km in altitude, we report here generally lower
507 water paths than in Mace and Avey (2017).

508 In Figure 4 we also show the uncertainty statistics in the retrieved microphysical
509 quantities. Consistent with our discussion of the case study in Figure 2, we find that LWP and
510 r_e are retrieved typically to within a few tens of percent while N_d is not known to within a factor
511 of 2 generally. The high uncertainty in N_d is expected. Being the zeroth moment of the DSD, N_d
512 is not directly constrained by any of the remote sensing measurements. β_{obs} being a function of
513 the 2nd moment of the DSD comes closest but even β_{obs} is still two orders removed meaning
514 that the droplet sizes in the DSD that control N_d are typically not those that control the cross
515 sectional area and β_{obs} . Constraining cross sectional area simply does not constrain N_d without
516 additional assumptions regarding correlations among the DSD moments. We, therefore, rely on
517 the correlations among the microphysical quantities to derive N_d . The natural variability in the
518 covariances that exist in the prior data combined with uncertainties in the retrieved quantities
519 drive the resulting uncertainty in N_d that is shown in Figure 4.

520 We use solar radiation measured at the surface as a means of vicarious validation of the
521 retrieved microphysics. Following the method described in Berry et al., (2019 and 2020), we

522 calculate the downwelling solar flux at the surface using the two-stream radiative transfer
523 model described by Toon et al. (1989) as modified by Kato et al. (2001). For solar zenith angles
524 less than 80° with no higher cloud layers, we compare the downwelling solar fluxes measured
525 on the ships with those calculated using the retrieved microphysical quantities. There are
526 challenges with such an approach since we are measuring the cloud properties at zenith and
527 then assuming that those properties are spread over a plane parallel sky. Our assumption is
528 that any significant biases in our retrievals would show up as overall biases in the solar flux
529 comparison. Using this method, we found extended periods when the flux was clearly biased
530 high or low over periods of hours. This caused us to remove 3 cases from the CAPRICORN I
531 data, 6 cases days from the CAPRICORN II data, and 4 case days from the MARCUS data set due
532 to large biases in fluxes. In most of these poorly rendered cases it seems that the MWR or
533 radar radome or both were wetted by precipitation or sea spray and/or the lidar window was
534 covered by condensed sea salt – operating sensitive instrumentation at sea in the Southern
535 Ocean is challenging. We conducted this manual filtering on daily timescales. If a day appeared
536 on average reasonably unbiased, we kept that day in the data set. What we find after removing
537 obviously bad days is that the flux difference (calculated flux minus observed flux) has a modal
538 value at -4 W m^{-2} with a mean, median and standard deviation of 25, 18, and 63 W m^{-2}
539 respectively (Fig. 4g). Because the low-level clouds are typically cellular even when overcast
540 and allow for variable transmission of sunlight and three dimensional radiative effects, it is not
541 unexpected that the bias is negative at higher values of flux. This is indicative of direct beam
542 sunlight reaching the pyranometers at higher zenith angles and/or reflection from cloud sides.
543 See also the negative solar forcing in the red histogram derived from the observed fluxes in
544 Figure 4h as evidence of these 3d effects. While our goal is to show an unbiased comparison,
545 the distribution in Figure 4g has a -6% bias suggesting that the retrieved microphysical
546 properties are physically reasonable but with possible low (high) biases in LWP (r_e) or offsetting
547 biases in both that are unknown. Unfortunately, no airborne validation is available. While the
548 NCAR GV aircraft flew over the R/V Investigator several times during CAPRICORN II, these
549 instances occurred when the MWR was wet due to drizzle or sea spray and retrievals could not
550 be conducted.

551 As discussed in Protat et al. (2017), MBL clouds like those considered here have a
552 significant impact on the downwelling solar flux at the surface (Figure 4h) and top of
553 atmosphere (TOA, Figure 4i). Expressing the net solar cloud radiative effect (CRE) as one minus
554 the fraction of the downwelling cloudy flux divided by the clear sky solar flux, we find a mean
555 value of 0.52 with a standard deviation of 0.33. The effect of these clouds then is to remove
556 typically between $1/3$ and $2/3$ of the solar radiation from the net surface fluxes when they are
557 present. The solar forcing derived from the actual flux observations (normalized by the
558 calculated clear sky), shows a broader distribution that extends to negative values indicating
559 reflection from cloud sides but also reflection from and blocking of sunlight by the ship super
560 structure.

561 The effect of these clouds on the solar energy balance is realized at the TOA by albedos
562 (A) that average 0.47 with a standard deviation of 0.12. A question we address below in more
563 detail is the extent to which the radiative effects of these clouds are susceptible to changes in
564 microphysics. The scatter plot of A versus optical depth shows that the majority of these clouds
565 exist at optical depths that are lower than ~ 20 . For comparison, Painemal and Minnis (2012)

566 examine data from eastern ocean basin stratocumulus using geostationary data and find
567 significantly lower A (0.2-0.3) from lower LWP ($\sim 60 \text{ g m}^{-2}$) and higher N_d ($150\text{-}200 \text{ cm}^{-3}$). The
568 analysis of Abel et al (2010) of the SE Pacific stratocumulus data show that N_d tended to
569 decrease away from the coastal regions to values near 100 cm^{-3} while water paths also
570 increased to values in excess of 150 g m^{-2} . Lu et al. (2009) analyzing airborne stratocumulus
571 data offshore of California showed a similar tendency with lower N_d and larger r_e with distance
572 from the continental influences.

573 Additional understanding of the Southern Ocean clouds, the processes involved in their
574 maintenance, and the effects they impose on the energy balance can be gained by examining
575 relationships among the variables – in particular how the microphysics and radiative effects are
576 interrelated. This thinking has heritage back to at least Twomey (1977) who showed
577 fundamental dependencies of A on N_d , i.e. the Twomey Effect. Because A is a function of both
578 the amount of condensed water in the column and how that water is distributed into the DSD,
579 the relationships are not necessarily straightforward. Often microphysics derived from satellite
580 use absorbing and non-absorbing solar channels to retrieve optical depth and r_e with water
581 path derived from perhaps coaligned microwave radiometer measurements and N_d is further
582 derived from assumptions. Our observations are of higher spatial resolution with the LWP
583 constrained by the microwave radiometer, the cross-sectional area of the DSD constrained by
584 the lidar, and the droplet sizes constrained by the radar. While there are still significant
585 uncertainties in the results, these unique measurements combined with coincident aerosol
586 measurements allow us to explore the role of these clouds in the SO atmosphere and surface
587 energy balance.

588 Recently Gryspeerd et al. (2019) examined global MODIS retrievals and found, in
589 agreement with previous studies, that cloud LWP is nonmonotonically related to N_d with LWP
590 increasing for lower N_d due to precipitation suppression while at higher N_d , more rapid
591 evaporation with smaller r_e tends to cause water path to decrease with N_d . While our data
592 excludes precipitation, we do not control for the nearby presence of drizzle or snow. In other
593 words, the non-precipitating clouds we analyze could be associated with nearby precipitation
594 and their properties modulated by precipitation processes. In Figure 5b we plot the
595 relationship of LWP as a function of N_d and we color code the scatter plot by r_e as described in
596 the caption. There is a strong relationship between N_d and LWP for a given r_e with LWP
597 increasing with r_e for a given N_d but there is some range (i.e. freedom) for LWP to vary for a
598 given N_d, r_e pair. We note that this scatter plot looks nothing like those shown in Gryspeerd et
599 al. (2019) except that by binning the LWP as a function of N_d and then plotting the median value
600 of that LWP, we also find a relationship where LWP tends to increase with N_d until about 100
601 cm^{-3} when the tendency is for LWP to begin decreasing with N_d . The inflection point in N_d that
602 we find is larger than in Gryspeerd et al. (2019) but we can perhaps interpret the results
603 similarly. Mace and Avey (2017) found similar effects on a seasonal basis with A-Train where a
604 given precipitation rate required higher LWP at larger N_d .

605 While it seems that the LWP can be modulated by the properties of the DSD, it is the
606 LWP that largely controls the effect of the clouds on the energy budget through A and surface
607 solar effect. This property is illustrated in Figure 5c and d where we plot A as a function of N_d
608 and visible optical depth τ with the LWP color coded as in Figure 5b and r_e color coded in Figure
609 5c. A increases with water path while the smaller r_e clouds tend to be associated with the

610 higher optical depths and larger A . Simply linearly regressing A as a function of N_d in the LWP
611 ranges for the colored points in Figure 5b, we find that within a given LWP range, A tends to
612 increase as N_d increases because increasing N_d is associated with decreasing r_e – although the
613 primary factor in determining A remains the LWP. The positive slopes on these regression
614 curves have been studied as the albedo susceptibility (Platnick and Twomey, 1994). Painemal
615 and Minnis (2012) define the albedo susceptibility $S_R = \frac{dA}{d \ln N_d}$ and it is determined using the
616 linear regression slope A with N_d within LWP bins as in Figure 5b. S_R is plotted for the SO liquid
617 phase clouds in Figure 5a. We find values of S_R that are generally smaller than those found by
618 Painemal and Minnis (2012) in the marine stratocumulus regions. Approximately 90% of our
619 data have LWP greater than 20 g m^{-2} and less than about 250 g m^{-2} . Therefore, results outside
620 that range should be viewed with appropriate skepticism. At its maximum near 0.045 (0.055 in
621 the Southern region), the value of S_R implies that a doubling of N_d would result in about a 0.9%
622 (1.1%) increase in A . Painemal and Minnis (2012) find a similar pattern with a tendency for S_R
623 to have a maximum at approximately 50 g m^{-2} and then decrease towards larger LWP although
624 the decrease of S_R in the southern region is larger than in the more northern latitudes and
625 reaches a minimum at lower LWP. The decrease of S_R with LWP can be understood by
626 considering that the reflectance of a cloud layer tends to asymptote to a maximum value as the
627 optical depth increases beyond about 20. So, as the layer becomes optically thicker due to
628 higher LWP, the ability for the microphysics to influence A lessens and thus S_R decreases. These
629 results suggest that the Southern latitude domain reaches this saturation point at smaller LWP
630 meaning that the clouds A is less susceptible to microphysics overall. The 95% confidence
631 intervals in the regression slopes plotted on the figure show significant uncertainty especially in
632 the southern region. However, the systematic nature of the tendency of S_R with LWP provides
633 additional confidence in the overall results.

634

635

636 4.3 Latitudinal Variations

637

638 Based on the physical oceanography (i.e. Armour et al., 2016) and biology (e. g. Deppler
639 and Davidson, 2017; Krüger and Graßl, 2011; McCoy et al, 2015) of the SO, we further explore
640 the latitudinal variability in the combined liquid cloud data set. A convenient set of boundaries
641 that we impose is based on Deppler and Davidson (2017; their Figure 2) that shows clear
642 variations in Chlorophyll a in the longitudinal domain we consider. From the latitude of Hobart
643 to roughly 50°S , the ocean tends to have higher biological productivity and more quiescent
644 weather during the summer months. The sub Antarctic front near 50°S marks entry into the
645 Antarctic Circumpolar Current (ACC) and seasonal storm track with the climatological position
646 of the Sub Antarctic Circumpolar Current Front near 62.5°S at this longitude marking entry into
647 the Antarctic marginal seas. We will refer to these latitude bins as the northern (Hobart to
648 50°S), middle (50°S to 62.5°S), and southern (poleward of 62.5°S) analysis regions. Figure 6
649 summarizes the cloud and radiative properties of the non-precipitating liquid clouds observed
650 in these regions. Recall that the step increase in sulfate aerosol concentration and CCN and N_d
651 in the 29 January case study (Figure 2) occurred near 64°S .

652 The differences in cloud properties between the northern and middle regions are subtle.
653 Overall, we find somewhat higher LWP in the middle region compared to the northern region,
654 with two modes in the LWP distribution, the peak of the second mode corresponding well with
655 that of the southern region. While the modal values of the N_d and r_e distributions of the
656 northern and middle domains are similar, the N_d distribution of the middle domain is skewed to
657 smaller values and the r_e distribution is skewed to slightly higher values. While we do not show
658 it here in detail, these differences tend to be associated with cases collected during CAPRICORN
659 II early in the program close to Tasmania. During CAPRICORN I, several days early in that
660 program near 45°S had trajectories from the Australian continent, high aerosol and CCN
661 number concentrations and larger (smaller) N_d (r_e). Proximity to Australia influences the
662 aerosol properties of the northern domain. Also during CAPRICORN II the anomalously high SST
663 in the Tasman sea was associated with persistently hazy conditions and higher aerosol numbers
664 that largely returned to lower values over the middle latitude domain.

665 Of interest is the bimodal nature of the N_d and r_e distributions in the southern latitude
666 domain. The overall LWP distribution is skewed to larger values (Figure 6a). One of the modes
667 in the N_d and r_e southern domain's distributions is clearly very similar to the modal values in the
668 two more northerly domains. A second mode tends to have significantly higher N_d and much
669 lower r_e values more indicative of the latter portion of the January 29 case when sulfate aerosol
670 concentrations and CCN increased and cloud properties changed. In Figure 7, we show cloud
671 and radiation properties compiled from the period 2- 5 January 2018 when RSV Aurora Australis
672 was at Casey Station near 66°S and 110°E. There are 4050 30-second retrievals in these
673 distributions. We plot the in-situ distributions like in Figure 4 for reference to show how much
674 of a contrast these clouds presented to what was measured by the SOCRATES aircraft flights.
675 The LWP during this event was higher than average, in the 200-300 g m⁻² range, while the N_d
676 was often in excess of 300 cm⁻³ with r_e around 5 μm. Comparing our calculation of the
677 downwelling solar flux with the observations shows a distribution with a strong mode near zero
678 difference with a skew toward positive values indicating a bias in the high N_d tail of the
679 distribution. However, with a solar noon clear sky flux near 800 W m⁻², the total solar forcing on
680 this day was on the order of 500 W m⁻² suggesting that on average our estimates of the cloud
681 microphysics were within the uncertainties discussed earlier. Thus, we find evidence for strong
682 bimodality in cloud properties along the coast of East Antarctica where one mode has the
683 properties of marine clouds from farther north while another mode has quite high droplet
684 numbers more consistent with high CCN air. The high LWP of these events strongly imply that
685 suppression of precipitation was occurring in the high N_d droplet mode clouds.

686

687 4.4 Optical Depth-Temperature Response

688

689 As discussed recently in Terai et al. (2019; hereafter T19), there is a robust prediction
690 among climate models that middle and high latitude clouds will impose a negative feedback on
691 the climate system because these clouds will increase in optical thickness with warming thereby
692 becoming more reflective. T19 comprehensively describe a number of possible physical
693 mechanisms operating in middle latitude clouds that could cause them to either thicken or thin
694 with warming. These mechanisms include a phase feedback where ice precipitation would
695 decrease in tendency thereby causing clouds to have high liquid water paths and longer

696 lifetimes, a thickening due to the fact that the moist adiabatic lapse rate steepens with
697 warming, or due to increased inversion strengths. Mechanisms that cause clouds to thin with
698 increased temperature would occur due to more efficient cloud top drying or due to decoupling
699 of the boundary layer, allowing entrainment of dry free tropospheric air to erode the cloud
700 water path. All or most of these mechanisms are physically plausible and could work together
701 or counter to each other to form a net response. T19 examine ground-based measurements
702 from several middle and high latitude sites and find that the mechanisms that cause overall
703 thinning of clouds with warming are predominant. Huang et al. (2016) examine MODIS data
704 over the SO and find a measurable decline in cloud optical depth with increasing SST due mostly
705 to a decrease in LWP associated with a decrease in cloud top height.

706 Shown in Figure 8, we find a negative trend of -0.62 K^{-1} in cloud optical depth with
707 temperature. While the correlation coefficient is fairly weak at -0.18 , the tendency for the
708 optical depth to decrease with temperature is in agreement with T19 and Huang et al. (2016).
709 We found a margin of error at the 99% confidence level of 0.06 K^{-1} in the regression slope using
710 a standard methodology (Giles et al., 1988). For verification, we randomly removed half of the
711 $\sim 70,000$ measurements and recalculating the slope 1000 times reasonably replicating the
712 confidence interval of 0.06 K^{-1} . We find that the slope of this regression line results in a
713 decrease in optical depth of approximately a factor two over the temperature range of the
714 observations (255-285 K). The scatter and resulting low correlation in this relationship is not
715 unexpected given the highly varied meteorology and differences in background aerosol over a
716 seasonal cycle. That we see any coherent trend at all is remarkable. We examined the factors
717 that influence the optical depth and found no significant tendencies in r_e or N_d but the LWP had
718 a downward trend but with weaker statistical significance that seemed to be associated with a
719 decrease in cloud physical thickness over the temperature range considered. These results are
720 consistent with the findings of Huang et al. (2016). We consider these results to be also
721 consistent with the finding of T19 suggesting that enhanced drying within the cloud layer is
722 dominating other mechanisms although the data set is only marginally adequate in terms of
723 duration to address the underlying causal mechanisms of this finding. While we are not
724 necessarily suggesting that these results should be taken to confirm or negate a feedback
725 response, the results do point to such mechanisms at work in this region to modulate cloud
726 properties.

727

728 5. Summary and Conclusions

729

730 We have presented an analysis of data compiled over three ship-based field campaigns
731 in the Southern Ocean between East Antarctica and Hobart, Tasmania. The data were collected
732 aboard the Australian Research Vessels Investigator (CAPRICORN I and II) and RSV Aurora
733 Australis (MARCUS). The MARCUS program ran during the summer resupply of Casey, Davis,
734 Mawson, and Macquarie Island stations between November, 2017 and March 2018. The
735 CAPRICORN II campaign took place in conjunction with the NSF-funded SOCRATES aircraft
736 mission and was conducted over a six-week period from early January 2018 until late February
737 2018. The CAPRICORN I campaign took place in March and April, 2016 and was previously
738 reported on by Mace and Protat (2018a and b).

739 We examine the properties of non-precipitating liquid phase clouds. This genre of
740 clouds comprises nearly half of the MBL-based layers in the Southern Ocean between 40°S and
741 65°S based on analysis of satellite radar and lidar data (Table 1). Combining the observations
742 from the three measurement campaigns provides 480 hours of measurements in these clouds.
743 In addition to surface meteorology, radiation, and radiosonde soundings, the critical
744 measurements from the three campaigns that we use to characterize cloud properties consist
745 of zenith pointing W-Band radar, elastic lidar attenuated backscatter operating in the visible
746 during MARCUS and in the UV during CAPRICORN, and zenith viewing microwave brightness
747 temperatures at 31 GHz. Together, these measurements allow us to constrain the LWP,
748 effective radius (r_e) and cloud droplet number concentration N_d of the liquid non precipitating
749 clouds using an optimal estimation algorithm that uses prior information from aircraft data
750 collected during the SOCRATES campaign. Uncertainties in the retrieved quantities are within
751 20% for the LWP. N_d is much more difficult to constrain because it is the zeroth moment of the
752 droplet size distribution whereas the measurements tend to constrain higher order moments.
753 Uncertainties in r_e and N_d are typically 10% and 70% depending on whether the clouds have
754 measurable radar reflectivity since often the non-precipitating clouds fall below the detection
755 thresholds of the radars (~25% of the time during CAPRICORN and 12% of the time during
756 Marcus). In such circumstances the uncertainties in r_e rise to 50% and N_d to 120%.

757 Overall, the non-precipitating clouds that we examine over the summertime SO tend to
758 have LWP in the 100-200 g m⁻², r_e of 8.7 um and N_d near (90 cm⁻³) on average making the SO
759 clouds somewhat thicker with smaller r_e and higher N_d than their counterparts in the
760 subtropical stratocumulus regions. The cloud properties drive visible optical depths of between
761 20 and 30 with a mean of 27 that tend to remove on average approximately ½ of the
762 downwelling solar flux from what would occur at the surface with albedos typically near 0.5.
763 The clouds, while typically overcast in coverage, have significant structure horizontally and
764 result in 3D radiative effects that cause the surface flux to vary substantially.

765 Many of the characteristics we find in the SO clouds have also been reported in
766 stratocumulus clouds with subtle differences. For instance, we find that higher N_d clouds tend
767 to be associated with higher LWP values up to N_d of ~110 cm⁻³ beyond which the mean water
768 paths tend to decrease. Gryspeerd et al. (2019) associate this behavior with suppression of
769 precipitation – a process that Mace and Avey (2017) documented in SO clouds between
770 summer and winter. We also find that the tendency for albedo to be modulated by N_d is
771 somewhat smaller for the non-precipitating clouds over the SO than for similar clouds in the
772 eastern subtropical oceans because the clouds are generally thicker. We do find that the
773 albedo susceptibility decreases as the LWP increases to about 200 g m⁻² in agreement with
774 other studies (Painemal and Minnis, 2012) for subtropical stratocumulus. The clouds over the
775 SO also tend to have an optical depth response to temperature that is similar to findings
776 reported from Northern Hemisphere ground sites by Terai et al. (2019) and for SO clouds
777 analyzed from satellite by Huang et al. (2016) where the clouds tend to decrease in optical
778 depth with temperature by about 2% per Kelvin. While there is considerable scatter in this
779 relationship due to the underlying natural variability, these results have reasonable statistical
780 significance and seem to be due to a thinning of the geometrical cloud layer thickness with
781 temperature.

782 Perhaps most significantly, we find a bimodality in cloud properties along the coast of
783 East Antarctica with one cloud property mode exhibiting properties consistent with the
784 maritime clouds observed farther north. The other mode has much higher N_d , small r_e that,
785 through precipitation suppression, allow for higher LWP to be maintained along with a
786 concomitant increase in albedo and surface solar forcing. We document a transition in this
787 regime with a case study from CAPRICORN II on 29 January 2018 when cloud r_e and N_d
788 simultaneously decreased and increased substantially over the space of ~ 30 minutes. This
789 change was followed by a step change in the sulfate aerosol concentrations and CCN measured
790 at the surface one hour later. Compositional markers for continental aerosol were not
791 observed, indicating that these were pristine air masses not altered by land emissions.
792 Following this step change, the non-precipitating clouds retained these properties for
793 approximately 5 days while the aerosol number concentrations remained mostly elevated.
794 Another case at Casey station of very high N_d and small r_e clouds that persisted for several days
795 is also shown. While additional study is needed, this variability is consistent with there being
796 distinct air mass changes along the East-Antarctic coast associated with air that contains
797 significantly different aerosol characteristics. Such variability in aerosol has been documented
798 in previous field data by Humphries et al., (2016).

799 This work raises many questions regarding the properties and processes that modulate
800 cloudiness in the Southern Ocean. That we see such remarkable sensitivity of this cloud genre
801 to step changes in the background aerosol suggests that there is much to learn regarding
802 aerosol-cloud-precipitation interactions (ACI) by studying the air mass transitions that seem to
803 happen in this region. From a climatological standpoint, these results raise questions about the
804 role of biogenic aerosol modulating the seasonal aerosol background state of the entire SO
805 (McCoy et al., 2015; Mace and Avey, 2017). To what extent is the increase in summertime N_d
806 over the wider SO caused by the massive biological phytoplankton blooms concentrated along
807 the marginal seas of Antarctica (Shaw, 1987) or is there a general increase in biogenic aerosol
808 throughout the broader SO? Our data are limited by bracketing a summer season. What
809 happens, for instance, during fall as the biogenic emissions subside, and when during spring do
810 biogenic aerosol sources begin to impact cloud and precipitation properties? Is this transition
811 related to biogeochemical cycling of sulfur compounds in melting sea ice (Damm et al., 2016)?
812 It is well documented that the Southern Ocean is undergoing substantial changes with climate
813 change (Armour et al., 2016; Kennicut et al., 2014; Liu et al., 2018) and understanding the
814 implications of these changes require documentation and understanding of the processes
815 occurring in the high latitude regions of the SO.

816
817 Acknowledgements:

818 *This research was supported in part by BER Award DE-SC0018995 (GM and RH) and*
819 *NASA grants 80NSSC19K1251 (GM). This project received grant funding from the*
820 *Australian Government as part of the Antarctic Science Collaboration Initiative program. The*
821 *Australian Antarctic Program Partnership is led by the University of Tasmania, and includes the*
822 *Australian Antarctic Division, CSIRO Oceans and Atmosphere, Geoscience Australia, the*
823 *Bureau of Meteorology, the Tasmanian State Government and Australia's Integrated Marine*
824 *Observing System. (AP, SA, and RH) Technical, logistical, and ship support for MARCUS were*
825 *provided by the Australian Antarctic Division through Australia Antarctic Science projects 4292*

826 and 4387 and we thank Steven Whiteside, Lloyd Symonds, Rick van den Enden, Peter de Vries,
827 Chris Young and Chris Richards for assistance. The authors would like to thank the staff of the
828 Marine National Facility for providing the infrastructure and logistical and financial support for
829 the voyages of the RV Investigator. Funding for these voyages was provided by the Australian
830 Government and the U.S. Department of Energy. All data used in this study are available in
831 public archives. MARCUS data are available from the DOE ARM archive at
832 <https://adc.arm.gov/armlogin/login.jsp>, SOCRATES data are available at
833 <https://data.eol.ucar.edu/project/SOCRATES>, CAPRICORN I and II data are available at
834 <https://www.marlin.csiro.au/geonetwork/srv/eng/search#!c88d62e1-43a2-4790-9fe6-5e4be21023b9>.
835

836
837
838

839 References:

840

841 Abel, S. J., D. N. Walters, and G. Allen, 2010: Evaluation of stratocumulus cloud prediction in the
842 Met Office forecast model during VOCALW-REx. *Atmos. Chem. Phys.*, 10, 10541-10559.
843 Doi:10.5194/acp-10-10541-2010.

844 Alexander, S. P., & Protat, A. (2019): Vertical profiling of aerosols with a combined Raman-
845 elastic backscatter lidar in the remote Southern Ocean marine boundary layer (43–
846 66°S,132–150°E). *Journal of Geophysical Research: Atmospheres*, 124,12,107–12,125.
847 <https://doi.org/10.1029/2019JD030628>

848 Alexander, S. P., and A. Protat, 2018: Southern Ocean cloud properties as observed from the
849 surface and satellite. *J. Geophys. Res. Atmos.*, 123.
850 <https://doi.org/10.1002/2017JD026552>

851 Armour, K. C., J. Marshall, J. R. Scott, A. Donohoe, and E. R. Newsom, 2016: Southern Ocean
852 warming delayed by circumpolar upwelling and equatorward transport, *Nature*
853 *Geoscience*, doi: 10.1038/NGEO2731.

854 Ayers, G. P. and J. L. Gras, 1991: Seasonal relationship between cloud condensation nuclei and
855 aerosol methanesulphonate in marine air. *Nature*, 353, 834-835.

856 Berry, E., G. G. Mace, and A. Gettelman, 2019: Using A-Train Observations to evaluate cloud
857 occurrence and radiative effects in the Community Atmosphere Model during the
858 Southeast Asia summer monsoon. *J. Clim.*, 32, 4145-4165, DOI: 10.1175/JCLI-D-18-
859 0693.1.

860 Berry, E., G. G. Mace, and A. Gettelman, 2020, Using A-Train observations to evaluate East
861 Pacific cloud occurrence and radiative effect in the Community Atmosphere Model.
862 Journal of Climate, Accepted, doi: 10.1175/JCLI-D-19-870.1

863 Bodas-Salcedo, A., K. D. Williams, P. R. Field, and A. P. Lock, 2012: the surface downwelling solar
864 radiation surplus over the Southern Ocean in the Met Office Model: The role of
865 midlatitude cyclone clouds. Journal of Climate, 25, 7467-2498.

866 Bodas-Salcedo, A., K. D. Williams, M. A. Ringer, I. Beau, J. N. S. Cole, J. -L. Dufresne, T. Koshiro, B.
867 Stevens, Z. Wang, and T. Yokohata, 2014: Origins, of the solar radiation biases over the
868 Southern Ocean in CFMIP2 Models, Journal of Climate, 27, 41-57, DOI: 10.1175/JCLI-D-
869 13-00169.1

870 Bodas-Salcedo, A., P. Hill, K. Furtado, K. Williams, P. Field, J. Manners, P. Hyder, and S. Kato, 2016:
871 Large contribution of supercooled liquid clouds to the solar radiation budget of the
872 Southern Ocean. J. Climate. doi:10.1175/JCLI-D-15- 0564.1

873 Bodas-Salcedo, A., Mulcahy, J. P., Andrews, T., Williams, K. D., Ringer, M. A., Field, P. R., &
874 Elsaesser, G. S. (2019). Strong dependence of atmospheric feedbacks on mixed-phase
875 microphysics and aerosol-cloud interactions in HadGEM3. Journal of Advances in
876 Modeling Earth Systems, 11,1735–1758. <https://doi.org/10.1029/2019MS001688>

877 Damm, E., D. Nomura, A. Martin, G. S. Dieckmann, and K. M. Meiners, 2016: DMSP and DMS
878 cycling within Antarctic sea ice during the winter-spring transition. Deep-Sea Research II
879 131, 150-159, <http://dx.doi.org/10.1016.j.dsr2.2015.12.015>.

880 Deppeler SL and Davidson AT (2017) Southern Ocean Phytoplankton in a Changing Climate.
881 Front. Mar. Sci. 4:40.doi: 10.3389/fmars.2017.00040

882 Delanoë, J., et al. (2016), BASTA, a 95 GHz FMCW Doppler radar for cloud and fog studies, J.
883 Atmos. Oceanic Technol., 33, 1023–1038.

884 Fossum, K. N., J. Ovadnevaite, D. Ceburnis, M. Dall’Osto, S. Marullo, M. Bellaicco, R. Simo, D Liu,
885 M Flynn, A. Zuend, and C. O’Dowd, 2018: Summertime primary and secondary
886 contributions to Southern Ocean Cloud Condensation Nuclei, Scientific Reports, 8:
887 13844, doi:10.1038/s41598-018-32047-4.

888 Frey, W. R. and J. E. Kay, 2017: The influence of extratropical cloud phase and amount
889 feedbacks on climate sensitivity. Clim. Dyn. DOI: 10.1007/s00382-017-3796-5.

890 Fröhlich, R., Cubison, M. J., Slowik, J. G., Bukowiecki, N., Prévôt, A. S. H., Baltensperger, U.,
891 Schneider, J., Kimmel, J. R., Gonin, M., Rohner, U., Worsnop, D. R., and Jayne, J. T.: The
892 ToF-ACSM: a portable aerosol chemical speciation monitor with TOFMS detection,
893 Atmos. Meas. Tech., 6, 3225–3241, <https://doi.org/10.5194/amt-6-3225-2013>, 2013.

894 Gettelmen, A., C. G. Bardeen, C. S. McCluskey, E. Jarvinen, J. Stith, and C. Bretherton, 2020:
895 Simulating observations of Southern Ocean clouds and implications for climate.
896 Submitted to Journal of Geophysical Research.

897 Gordon, N. D., and S. A. Klein (2014), Low-cloud optical depth feedback in climate models, J.
898 Geophys. Res. Atmos., 119, 6052–6065, doi:10.1002/2013JD021052.

899 Giles, E. and Klepinger, L., "Confidence Intervals for Estimates Based on Linear Regression in
900 Forensic Anthropology," *Journal of Forensic Sciences*, Vol. 33, No. 5, 0, pp. 1218-
901 1222, <https://doi.org/10.1520/JFS12555J>. ISSN 0022-1198

902 Hu, Y., et al., 2009: CALIPSO/CALIOP cloud phase discrimination algorithm, Journal of
903 Atmospheric and Oceanic Technology, 26, 2293-2309, DOI: 10.1175/2009JTECHA1280.1

904 Hu, Y., S. Rodier, K-m. Xu, W. Sun, J. Huang, B. Lin, P. Zhai, and D. Josset, 2010: Occurrence,
905 liquid water content, and fraction of supercooled water clouds from combined
906 SALIOP/IIR/MODIS measurements. 2010: JOURNAL OF GEOPHYSICAL RESEARCH, VOL.
907 115, D00H34, doi:10.1029/2009JD012384, 2010

908 Huang, Y., S. T. Siems, M. J. Manton, D. Rosenfeld, R. Marchand, G. M. McFarquhar, and A.
909 Protat, 2016: What is the role of sea surface temperature in modulating cloud and
910 precipitation properties over the Southern Ocean? Journal of Climate, 29, 7453-7473,
911 doi: 10.1175/JCLI-D-15-0768.1

912 Humphries, R. S., A. R. Klekociuk, R. Schofield, M. Keywood, J. Ward, and S. R. Wilson, 2016:
913 Unexpectedly high ultrafine aerosol concentration above East Antarctic sea ice. Atmos.
914 Chem. Phys. 16, 2185-2206, doi:10.5192/acp-16-2185-2016.

915 Kay, J. E., Wall, C., Yettella, V., Medeiros, B. Hannay, C., P. Caldwell, and C. Bitz, 2016: Global
916 climate impacts of fixing the Southern Ocean shortwave radiation bias in the
917 Community Earth System Model, J. Climate, doi:10.1175/JCLI-D-15-0358.1

918 Kelleher, M. K., and K. M. Grise, 2019: Examining Southern Ocean Cloud Controlling Factors on
919 Daily time scales and their connections to midlatitude weather systems. Journal of
920 Climate, 32, 5145-5159, doi: 10.1175/JCLI-D-18-0840.1

921 Klein, S. A., A. Hall, J. R. Norris and R. Pincus, 2017: Low-cloud feedbacks from cloud-controlling
922 factors: A review. Surv. Geophys., 38, 1307-1329, [https://doi.org/10.1007/s10712-017-](https://doi.org/10.1007/s10712-017-9433.3)
923 [9433.3](https://doi.org/10.1007/s10712-017-9433.3).

924 Kato, S., G. L. Smith, and H. W. Barker, 2001: Gamma-weighted discrete ordinate two-stream
925 approximation for computation of domain-averaged solar irradiance. J. Atmos. Sci., 58,
926 3797-3803.

- 927 Kennicutt II, M. C., and Co-Authors, 2014: A roadmap for Antarctic and Southern Ocean science
928 for the next two decades and beyond, 2014: *Antarctic Science*, 27(1), 3-18.
- 929 Kirk, P. D. W., M. P. H. Stumpf, 2009: Gaussian process regression bootstrapping: Exploring the
930 effects of uncertainty in time course data. *Bioinformatics*, 25, 1300-1306.
- 931 Klepp, C., S. Michel, A. Protat, J. Burdanowitz, N. Albern, A. Dahl, M. Kähnert, V. Louf, S. Bakan,
932 and S. A. Buehler, 2018: OceanRAIN, a new in-situ shipboard global ocean surface-
933 reference dataset of all water cycle components. *Nature – Scientific Data*, DOI:
934 10.1038/sdata.2018.122.
- 935 Kollias, P., B. P. Treserras, and A., Protat, 2019: Calibration of the 2007-2017 record of ARM
936 cloud radar observations using CloudSat. *Atmos. Meas. Tech.* 12, 4949-4964,
937 <https://doi.org/10.5194/amt-12-4949-2019>.
- 938 Krüger, O., and H. Graßl, 2011: Southern Ocean phytoplankton increases cloud albedo and
939 reduces precipitation, *Geophysical Research Letters*, 38, L08809, DOI:
940 10.1029/2011GL047116.
- 941 Li, J. Y. Hu., J. Huang, K. Stamnes, Y. Yi, and S. Stamnes, 2011: A new method for retrieval of the
942 extinction coefficient of water clouds by using the tail of the CALIOP signal. *Atmos.*
943 *Chem. Phys.*, 11, 2903-2916, doi: 10.5194/acp-11-2903-2011.
- 944 Liljegren, J. C., 1994: Two-channel microwave radiometer for observations of total column
945 precipitable water vapor and cloud liquid water path, paper presented at the Fifth
946 Symposium on Global Change Studies, Am. Meteorol. Soc., Nashville, Tenn. Jan. 23-28.
- 947 Liljegren, J. C., E. E. Clothiaux, G. G. Mace, S. Kato, X. Dong, 2001: A new retrieval for cloud
948 liquid water path using a ground-based microwave radiometer and measurements of
949 cloud temperature. *Journal of Geophysical Research*, Vol. 106, No. D13, 14,485-14,500.
- 950 Liu, W. J. Lu, S.-P. Xie, and Alexey Fedorov, 2018: Southern Ocean heat uptake, redistribution
951 and storage in a warming climate: The role of meridional overturning circulation. *Journal*
952 *of Climate*, 31, 4727-4743, DOI: 10.1175/JCLI-D-17-07061.1.
- 953 Lu, M.-L. and A. Sorooshian, H. H. Jonsson, G. Feingold, R. C. Flagan, J. H. Seinfeld, Marine
954 stratocumulus aerosol-cloud relationships in the MASE II experiment: Precipitation
955 susceptibility in Eastern Pacific marine stratocumulus, *Journal of Geophysical Research*,
956 114, doi:10.1029/2009JD012774.
- 957 Mace, G. G., Sally Benson, and Y. Hu, 2020: On the frequency of the occurrence of the ice phase
958 in supercooled Southern Ocean low clouds derived from CALIPSO and CloudSat.
959 *Geophysical Research Letters*, In press, <https://doi.org/10.1029/2020GL087554>.

- 960 Mace, G. G., and S. Avey, 2017: Seasonal variability of warm boundary layer clouds and
961 precipitation properties in the Southern Ocean as diagnosed from A-Train data. *Journal*
962 *of Geophysical Res. Atmos.*, 122, 1015-1032, doi:10.1002/2016JD025348.
- 963 Mace, G. G., Q Zhang, M. Vaughn, R. Marchand, G. Stephens, C. Trepte, D. Winker, 2009: A
964 description of hydrometeor layer occurrence statistics derived from the first year of
965 merged Cloudsat and CALIPSO data. *J. Geophys. Res.*, 114,D00A26,
966 doi:10.1029/2007JD009755.
- 967 Mace G. G., 2010: Cloud properties and radiative forcing over the maritime storm tracks of the
968 Southern Ocean and North Atlantic derived from A-Train. *Journal of Geophysical*
969 *Research*, 115, doi:10.1029/2009JD012517.
- 970 Mace, G. G. and Zhang, 2014: The Cloudsat Radar-Lidar Geometrical Profile Algorithm (RL-
971 GeoProf): Updates, Improvements, and Selected Results. *Journal of Geophysical*
972 *Research*, DOI: 10.1002/2013JD021374.
- 973 Mace G. G., and B. Berry, 2017: Using active remote sensors to evaluate cloud-climate
974 feedbacks: A review and and look to the future. *Current Climate Change Reports*, DOI
975 10.1007/s40641-017-0067-9.
- 976 Mace, G. G., S. Avey, S. Cooper, M. Lebsock, S. Tanelli, and G. Dobrowalski, 2016: Retrieving co-
977 occurring cloud and precipitation properties of warm marine boundary layer clouds with
978 A-Train data. *J. Geophys. Res.* 120, doi:10.1002:/2015JDO23681.
- 979 Marchand, R., G. G. Mace, T. Ackerman, and G. Stephens, 2008: Hydrometeor detection using
980 CloudSat – an Earth-orbiting 94-GHz cloud radar. *Journal of Atmospheric and Oceanic*
981 *Technology*. 25, doi:10.1175/2007JTECHA1006.1, 519-533.
- 982 Maahn, Masimillian, D. D. Turner, U. Lohnert, D. J. Posselt, Kerstin Ebell, G. G. Mace, and J. M.
983 Comstock. 2020: Optimal estimation retrievals and their uncertainties: What every
984 atmospheric scientist should know. *Bull. Amer. Meteor. Soc.*
985 <https://doi.org/10.1175/BAMS-D-19-0027.1>.
- 986 McCoy D. T., S. M. Burrows, R. Wood, D. P. Grosvenor, S. M. Elliott, P. Ma, P. J. Rasch, and D.
987 Hartmann, 2015: Natural aerosols explain seasonal and spatial patterns of Southern
988 Ocean cloud albedo. *Sci. Adv.* 1, e1500157.
- 989 McCoy D. T., P. R. Field, G. S. Elsaesser, A. Bodas-Salcedo, B. H. Kahn, M, D. Zelinka, C. Kodama,
990 T. Mauritsen B. Vanniere, M. Roberts, P. L. Vidale, D. Saint-Martin, A. Voldoire, R.
991 Haarsma, A. Hill, B. Shipway, and J. Wilkonson, 2019: Cloud feedbacks in extratropical
992 cyclones: Insights from long-term satellite data and high resolution global simulations.
993 *Atmos. Chem. Phys.*, 19, 1147-1172, <https://doi.org/10.5194/acp-19-1147-2019>.

- 994 McFarquhar, G. and 42 coauthors, 2020: Unique observations of clouds, aerosols, precipitation,
 995 and surface radiation over the Southern Ocean: An overview of CAPRICORN, MARCUS,
 996 MICRE, and SOCRATES. Submitted to the Bulletin of the American Meteorological Society.
- 997 O'Connor, E. J., et al., (2004): A technique for autocalibration of cloud lidar, *J. Atmos. Oceanic*
 998 *Technol.*, 21, 777-786.
- 999 Painemal, D. and P. Zuidema, 2013: The first aerosol indirect effect quantified through airborne
 1000 remote sensing during VOCALS-Rex. *Atmos. Chem. Phys.* 13, 917-931, doi:10.5194/acp-
 1001 13-917-2013.
- 1002 Painemal, D. and P. Minnins, 2012: On the dependence of albedo on cloud microphysics over
 1003 marine stratocumulus clouds regimes determined from Clouds and the Earth's Radiant
 1004 Energy System (CERES) data. *Journal of Geophysical Research*, 117, D06203,
 1005 doi:10.1029/2011JD017120.
- 1006 Platnick, S., and S. Twomey, 1994: Determining the susceptibility of cloud albedo to changes in
 1007 droplet concentration with Advanced Very High Resolution Radiometer. *Journal of*
 1008 *Applied Meteorology*, 33, 334-347.
- 1009 Platt, C. M. R., D. M. Winker, M. A. Vaughan, and S. D. Miller, 1999: Backscatter-to-extinction
 1010 ratios in the top layers of tropical mesoscale convective systems and in isolated cirrus
 1011 from LITE observations. *Journal of Applied Meteorology*, 38, 1330-1345.
- 1012 Protat, A., E. Schulz, L. Rikus, Z. Sun, and Y. Xiao, 2017: Shipborne observations of the radiative
 1013 effect of Southern Ocean Clouds. *J. Geophys. Res. Atmos.*, 122, 318-328.
- 1014 Protat, A., D. Bouniol, E. J. O'Connor, H. K. Baltink, J. Verlinde, and K. Widener, 2011: CloudSat as
 1015 a Global Radar Calibrator. *J. Atmos. Oceanic Tech.*, 28, 445-452.
- 1016 Rauber, R. M. and co-authors, 2006: Rain in shallow cumulus over the ocean; the RICO campaign.
 1017 *Bulletin of the American Meteorological Society*, 87, 1912-1919.
- 1018 Royer, P., A. Bizard, L. Sauvage, and L. Thobois, 2014: Validation protocol and intercomparison
 1019 campaigns with the R-MAN510 aerosol lidar. *Proc. 17th Int. Symp. for the Advancement*
 1020 *of Boundary-Layer Remote Sensing, Auckland, New Zealand, ISARS, XX-XX.*
- 1021 Savic-Jovcic, V. and B. Stevens, 2008: The structure and mesoscale organization of precipitating
 1022 stratocumulus. *J. Atmos. Sciences*, 65, 1587-1605.
- 1023 Schulz, E. W., S. A. Josey, and R. Verein, 2012: First air-sea flux mooring measurements in the
 1024 Southern Ocean, *Geophysical Research Letters*, 39, doi. 10.1029/2012GL052290.
- 1025 Shaw G. E. 1988: Antarctic Aerosols: A Review. *Reviews of Geophysics*, 26, 1, 89-112.

- 1026 Stephens, G. L., et al. (2008), CloudSat mission: Performance and early science after the first year
1027 of operation, *J. Geophys. Res.*, 113, D00A18, doi:10.1029/2008JD009982.
- 1028 Tan, I., T. Storelvmo, and M. D. Zelinka, 2016: Observational constraints on mixed phase clouds
1029 imply higher climate sensitivity. *Science*, 352, 224-228, doi: 10.1126/science.aad5300.
- 1030 Tanelli, S., S. L. Durden, E. Im, K. S. Pak, D. G. Reinke, P. Partain, J. M. Haynes, and R. T.
1031 Marchand, 2008: CloudSat's Cloud Profiling Radar after two years in orbit: Performance,
1032 calibration, and processing. *IEEE Transaction on Geoscience and Remote Sensing*, 46,
1033 3650-3663, DOI: 10.1109/TGRS.2008.2002030.
- 1034 Terai, C. R., Zhang, Y., Klein, S. A., Zelinka, M. D., Chiu, J. C., & Min, Q. (2019). Mechanisms
1035 behind the extratropical stratiform low-cloud optical depth response to temperature in
1036 ARM site observations. *Journal of Geophysical Research: Atmospheres*, 124, 2127–2147.
1037 <https://doi.org/10.1029/2018JD029359>
- 1038 Toon, O. B., C. P. McCay, T. P. Ackerman, and K. Santhanam, 1989: Rapid calculation of radiative
1039 heating rate and photodissociation rates in inhomogeneous multiple scattering
1040 atmospheres. *J. Geophys. Res.*, 94, 16,287-16,301.
- 1041 Trenberth, Kevin E., John T. Fasullo, 2010: Simulation of Present-Day and Twenty-First-Century
1042 Energy Budgets of the Southern Oceans. *J. Climate*, 23, 440–454. DOI
1043 10.1175/2009JCLI3152.1
- 1044 Twomey, S. 1977: The influence of pollution on the shortwave albedo of clouds. *Journal of the*
1045 *Atmospheric Sciences*, 34, 1149-1152.
- 1046 Vergara-Temprado, J., A. K. Miltenberger, K. Furtado, D. P. Grosvenor, B. J. Shipway, A. A. Hill, J.
1047 M. Wilkinson, P. R. Field, B. J. Murray, and K. S. Carslaw, 2018: Strong control of
1048 Southern Ocean cloud reflectivity by ice nucleating particles. *Proceedings of the*
1049 *National Academy of Sciences*, doi: 10.1073/pnas.1721627115.
- 1050 Wang, Y., G. M. McFarquhar, R. M. Rauber, C. Zhao, W. Wu, J. A. Finlon, D. M. Stechman, J.
1051 Stith, J. B. Jensen, M. Schnaiter, E. Jarvinen, F. Waitz, J. Vivekanandan, M. Dixon, B.
1052 Rainwater, and D. W. Twohy, 2020: Microphysical properties of generating cells over the
1053 Southern Ocean: Results from SOCRATES. *Accepted Journal of Geophysical Research*.
- 1054 Winker, D. M., M. A. Vaughan, A. Omar, Y. Hu, K. Powell, Z. Liu, W. H. Hunt, S. A. Young, 2009:
1055 Overview of the CALIPSO mission and CALIOP data processing algorithms. *Journal of*
1056 *Atmospheric and Oceanic Technology*, 26, 2310-2324, DOI: 10.1175/2009JtechA1281.1
- 1057 Zuidema, P., Xue, H., & Feingold, G. (2008). Shortwave radiative impacts from aerosol effects on
1058 marine shallow cumuli. *Journal of the Atmospheric Sciences*, 65(6), 1979-
1059 1990. <https://doi.org/10.1175/2007JAS2447.1>

1060

1061 Table Captions:

1062 Table 1: Table 1: Vertical occurrence data from CloudSat (Stephens et al., 2008) and CALIPSO
1063 (Winker et al., 2009) between 2007-2010 using the combined characterization of Mace and
1064 Zhang, (2014) in the 40s-70s latitude belt.

1065

1066 Figure Captions:

1067 Figure 1. Voyage tracks taken R/V Investigator and Aurora Australis during CAPRICORN I and II
1068 and MARCUS

1069 Figure 2. January 29 Case Study collected during CAPRICORN II. a) radar reflectivity from the
1070 BASTA W-Band Radar. Lidar derived cloud base is marked by white dots. b) Lidar attenuated
1071 backscatter, c) lidar layer-integrated depolarization ratio (red) and multiple scattering factor
1072 (black), d) difference of 31 GHz Tb from cloud-free sky (black) and lidar depolarization ratio at
1073 cloud base. e) Retrieved Liquid water path with uncertainty marked by the error bars. f)
1074 retrieved effective radius with error bars. g) retrieved cloud droplet number with error bars. h)
1075 Aerosol Sulfate mass and CCN at 0.5% supersaturation.

1076 Figure 3. Comparison of sub cloud radar reflectivity from liquid hydrometeors observed by the
1077 calibrated BASTA W-Band radar and the MARCUS MWACR during the months of January and
1078 February (red).

1079 Figure 4. Cloud and radiation property frequency distributions compiled from the retrieved
1080 microphysical properties using data from MARCUS and CAPRICORN I and II. Red histograms
1081 show observations compiled from in situ airborne data from SOCRATES (b and c) and from the
1082 ship pyranometer (h). a) Liquid water path, b) Effective radius with red showing the effective
1083 radius frequency from the SOCRATES in situ data c) Cloud Droplet Number Concentration with
1084 red as in b. d) uncertainty distribution of LWP, e) uncertainty distribution of effective radius, f)
1085 uncertainty distribution of cloud droplet number. g) Distribution of the difference of calculated
1086 downwelling solar flux from that observed at the ship. h) Calculated fraction of the downwelling
1087 solar flux at the surface removed from the clear sky flux by the clouds. I) scatterplot of albedo
1088 calculated from the cloud properties as a function of visible optical depth.

1089 Figure 5. Derived cloud and radiation properties. a) Albedo Susceptibility. Red shows southern
1090 analysis domain. Black shows middle and northern domains combined. Error bars show 95%
1091 confidence interval of the linear regression slope. b) liquid water path as a function cloud
1092 droplet number concentration color coded by effective radius with black: sub 5 um, blue: 5-7
1093 um, red: 7-9 um, orange: 9-11 um), yellow: > 11 um. The black curve with symbols show the
1094 mean LWP in cloud droplet number bins. b) Albedo Susceptibility ($dA/d\ln(Nd)$). Red is the

1095 southern analysis domain. Black is the northern and middle domains. c) Albedo as function of
1096 optical depth with color coded re as in a. d) Albedo as a function of Nd color coded for LWP
1097 with black less than 50 g m⁻², blue denotes LWP from 50-100 g m⁻², and orange denotes LWP
1098 from 100 to 150 g m⁻². The lines denote linear regressions of albedo as a function of Nd in the
1099 LWP bins representing the albedo susceptibility as depicted in a.

1100 Figure 6. Latitudinal variations of retrieved cloud and derived radiative properties. solid black
1101 denotes the northern analysis domain. Dashed denotes the middle latitude domain. Red
1102 denotes the Southern Latitude domain. See text for details

1103 Figure 7. As in Figure 4 except for the 2-5 January 2018 Marcus Case Study when the Aurora
1104 Australis was docked at Casey Station Antarctica.

1105 Figure 8. Regression of visible optical depth of the liquid phase non precipitating clouds as a
1106 function of layer temperature for the combined Capricorn and Marcus data sets.
1107

1108

1109

1110

1111

1112

1113

1114

1115

1116

1117

1118

1119

1120

1121

1122

1123

1124

1125

1126

1127

1128

1129

1130

1131

1132

1133

1134

1135

1136

1137

1138

1139

1140

1141

Capricorn 1 - · - · -
20160313-20160413

Marcus - - -
20171101-20180325

Capricorn 2 —
20180110-20180221

Nov Dec Jan Feb Mar Apr

45°S
50°S

140°E 145°E 150°E

40°S
50°S
60°S
70°S

60°E 75°E 90°E 105°E 120°E 135°E 150°E 165°E

Figure 1. Voyage tracks taken R/V Investigator and Aurora Australis during CAPRICORN I and II and MARCUS

30

1142
1143
1144

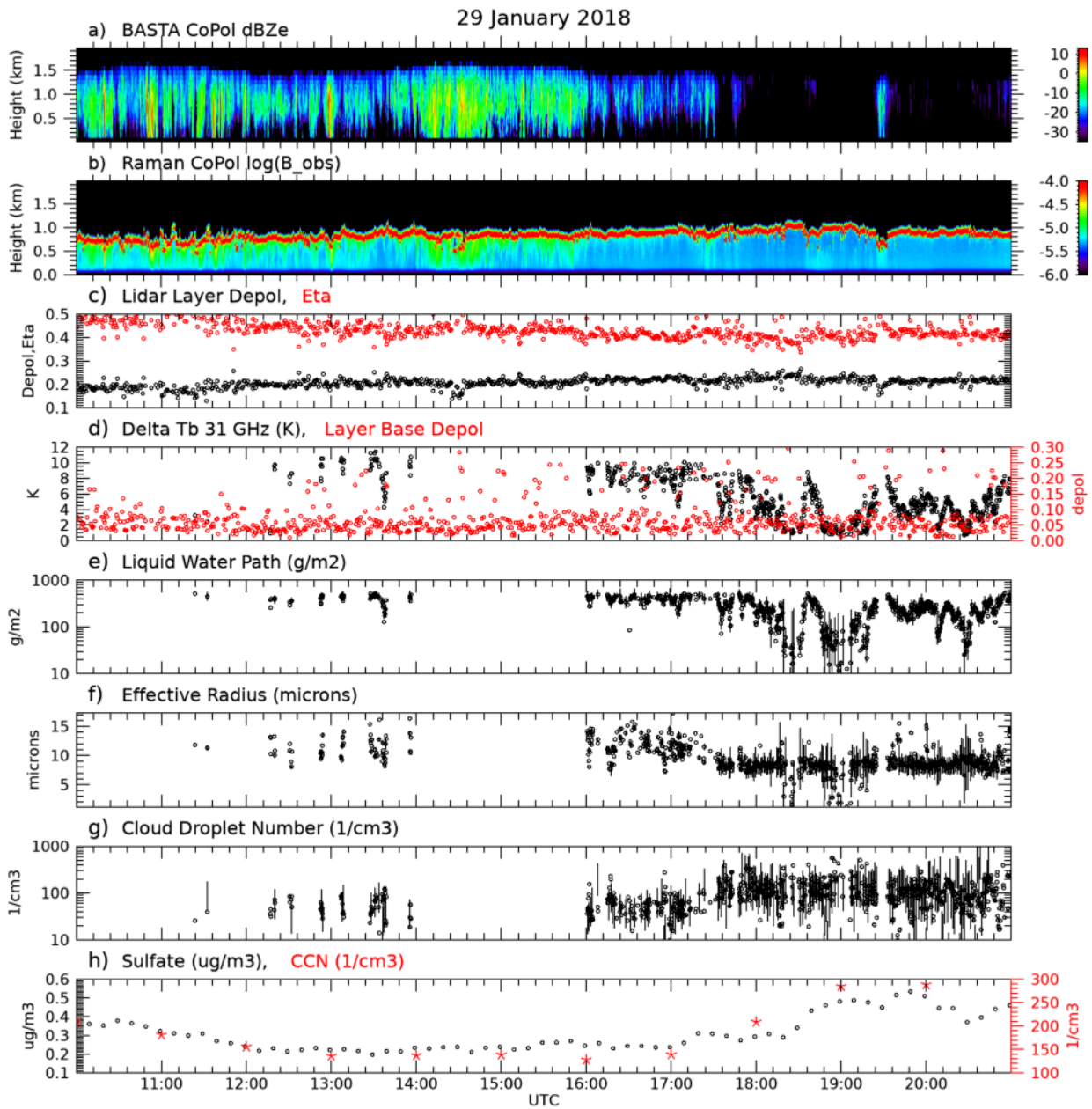


Figure 2. January 29 Case Study collected during CAPRICORN II. a) radar reflectivity from the BASTA W-Band Radar. Lidar derived cloud base is marked by white dots. b) Lidar attenuated backscatter, c) lidar layer-integrated depolarization ratio (red) and multiple scattering factor (black), d) difference of 31 GHz Tb from cloud-free sky (black) and lidar depolarization ratio at cloud base. e) Retrieved Liquid water path with uncertainty marked by the error bars. f) retrieved effective radius with error bars. g) retrieved cloud droplet number with error bars. h) Aerosol Sulfate mass and CCN at 0.5% supersaturation.

1145
1146
1147

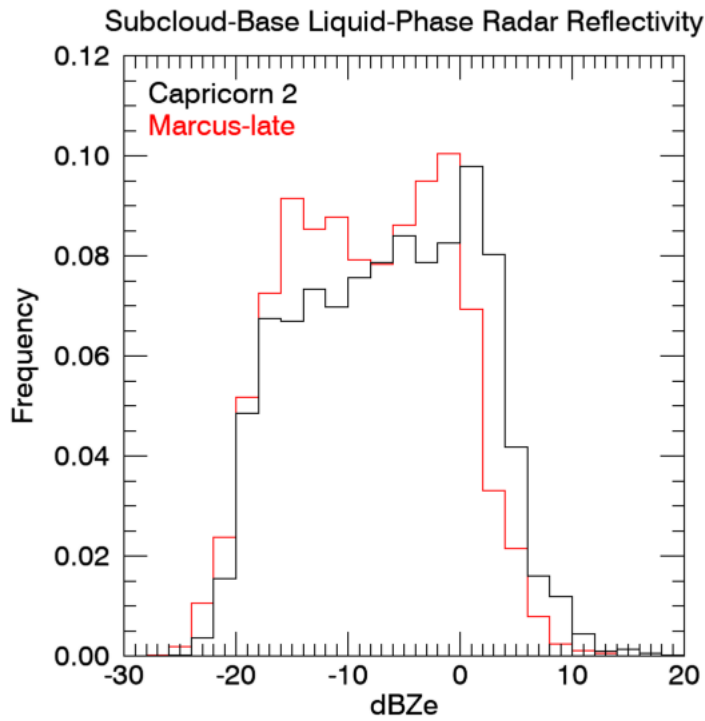


Figure 3. Comparison of sub cloud radar reflectivity from liquid hydrometeors observed by the calibrated BASTA W-Band radar and the MARCUS MWACR during the months of January and February (red).

1148
1149
1150

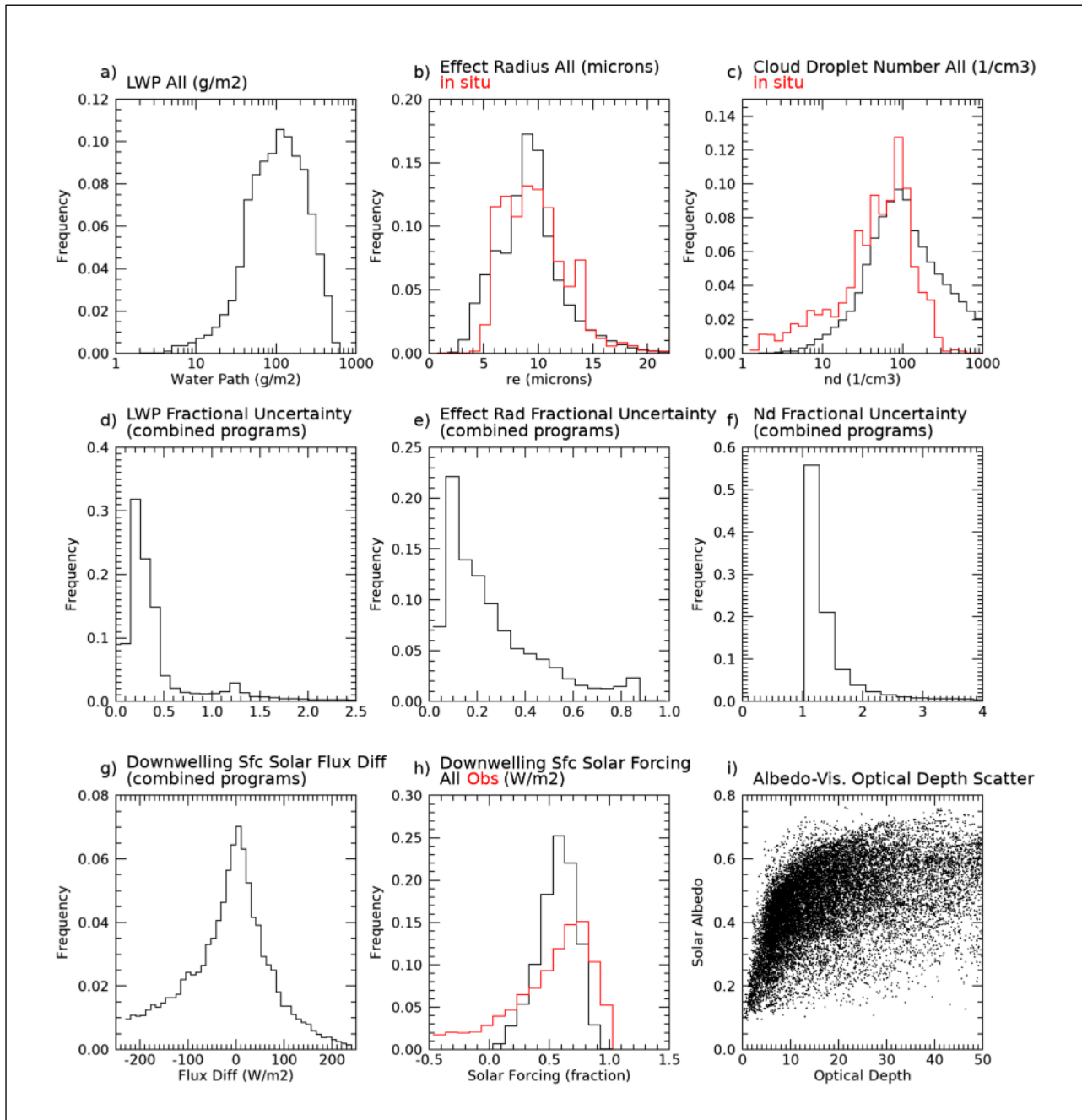


Figure 4. Cloud and radiation property frequency distributions compiled from the retrieved microphysical properties using data from MARCUS and CAPRICORN I and II. Red histograms show observations compiled from in situ airborne data from SOCRATES (b and c) and from the ship pyranometer (h). a) Liquid water path, b) Effective radius with red showing the effective radius frequency from the SOCRATES in situ data c) Cloud Droplet Number Concentration with red as in b. d) uncertainty distribution of LWP, e) uncertainty distribution of effective radius, f) uncertainty distribution of cloud droplet number. g) Distribution of the difference of calculated downwelling solar flux from that observed at the ship. h) Calculated fraction of the downwelling solar flux at the surface removed from the clear sky flux by the clouds. i) scatterplot of albedo calculated from the cloud properties as a function of visible optical depth.

1151
1152
1153
1154

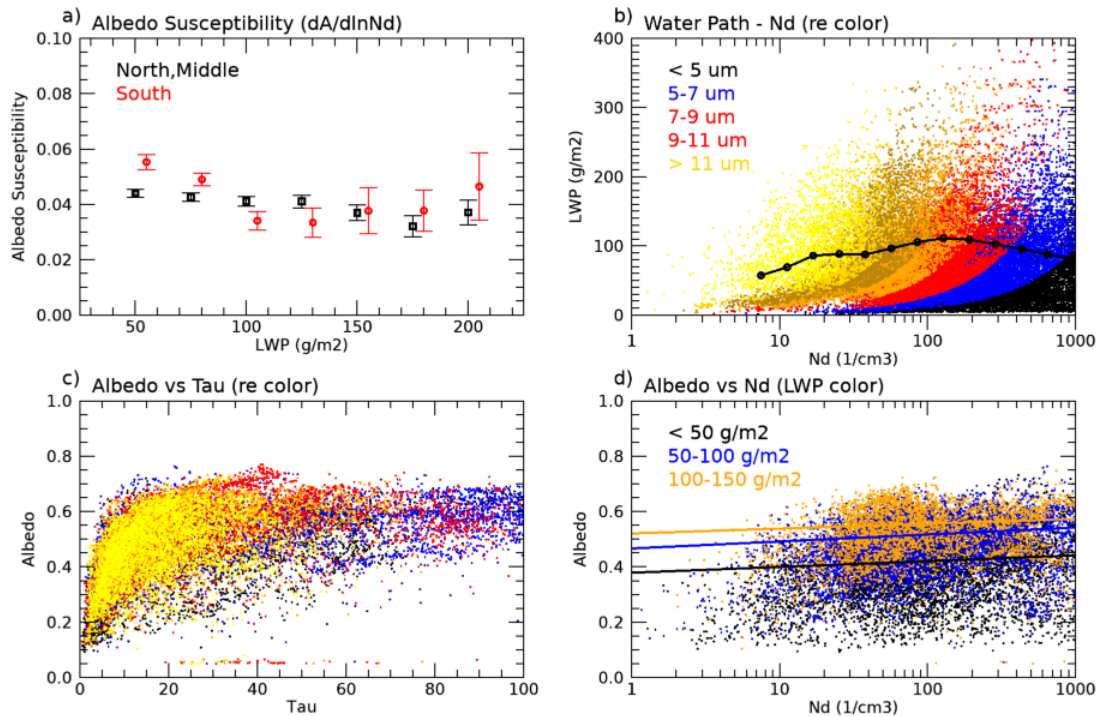


Figure 5. Derived cloud and radiation properties. a) Albedo Susceptibility. Red shows southern analysis domain. Black shows middle and northern domains combined. Error bars show 95% confidence interval of the linear regression slope. b) liquid water path as a function cloud droplet number concentration color coded by effective radius with black: sub 5 μm, blue: 5-7 μm, red: 7-9 μm, orange: 9-11 μm, yellow: > 11 μm. The black curve with symbols show the mean LWP in cloud droplet number bins. b) Albedo Susceptibility ($dA/d\ln(Nd)$). Red is the southern analysis domain. Black is the northern and middle domains. c) Albedo as function of optical depth with color coded re as in a. d) Albedo as a function of Nd color coded for LWP with black less than 50 g m⁻², blue denotes LWP from 50-100 g m⁻², and orange denotes LWP from 100 to 150 g m⁻². The lines denote linear regressions of albedo as a function of Nd in the LWP bins representing the albedo susceptibility as depicted in a.

1155
1156
1157
1158

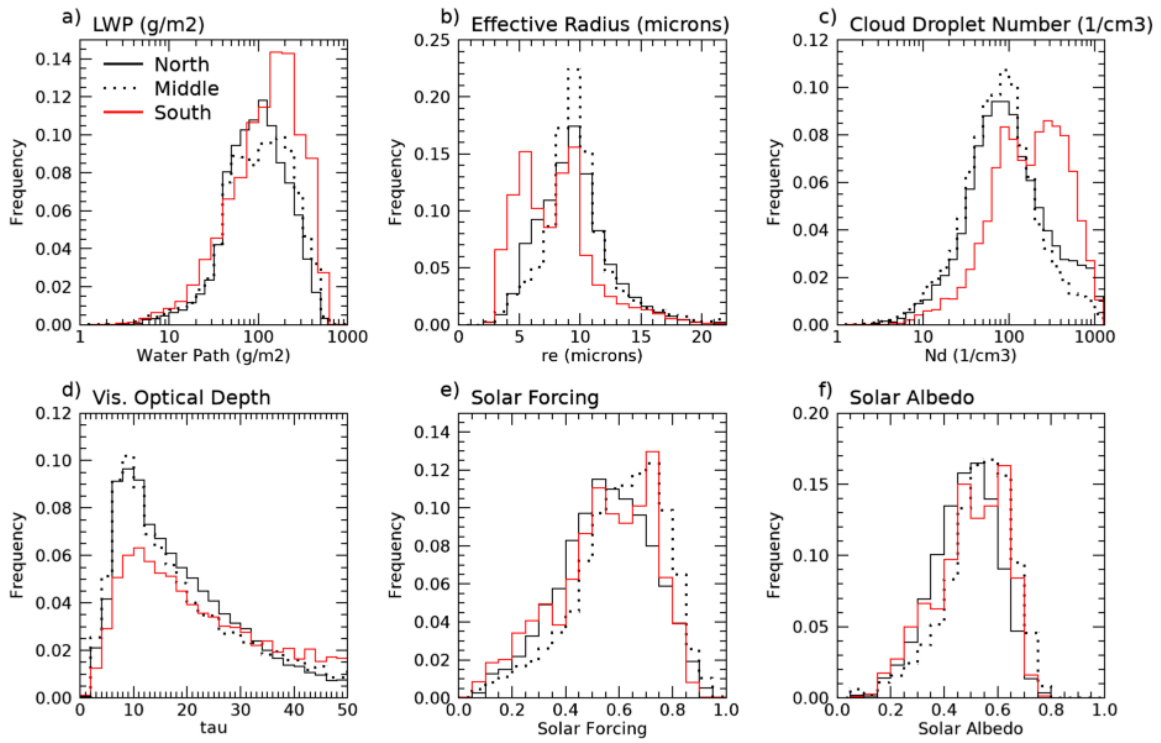


Figure 6. Latitudinal variations of retrieved cloud and derived radiative properties. solid black denotes the northern analysis domain. Dashed denotes the middle latitude domain. Red denotes the Southern Latitude domain. See text for details

1159
1160
1161

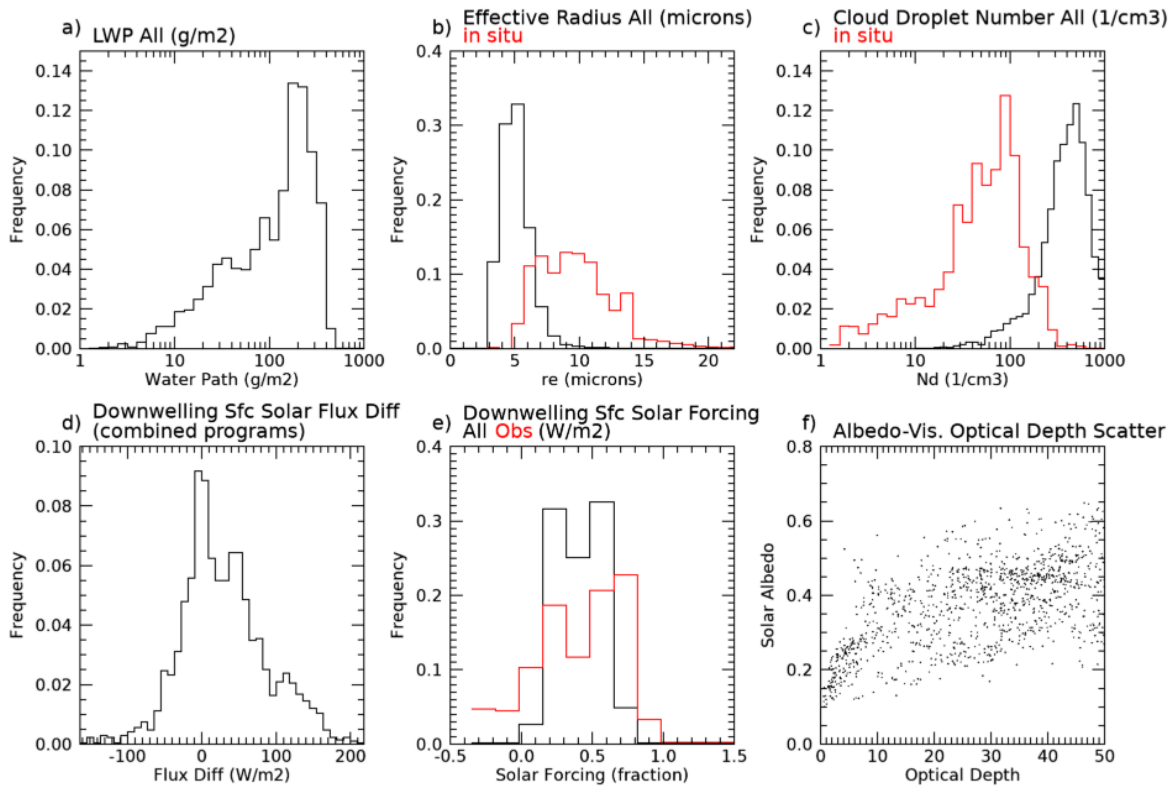


Figure 7. As in Figure 4 except for the 2-5 January 2018 Marcus Case Study when the Aurora Australis was docked at Casey Station Antarctica.

1162
1163
1164

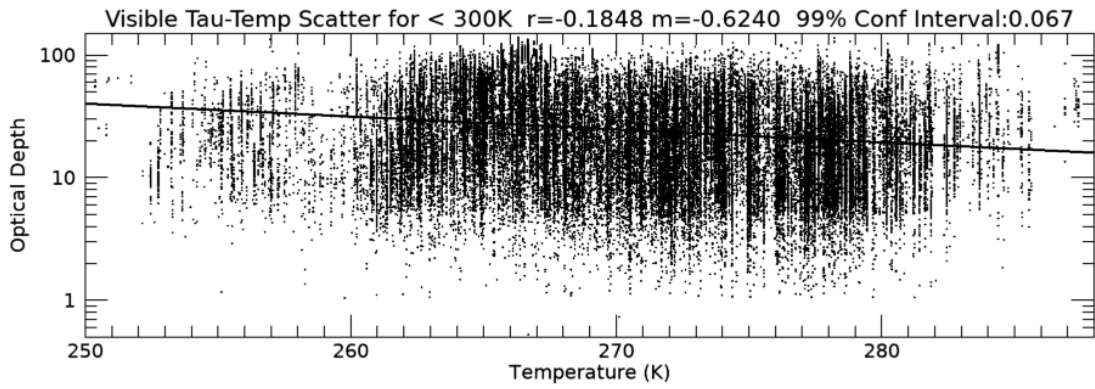


Figure 8. Regression of visible optical depth of the liquid phase non precipitating clouds as a function of layer temperature for the combined Capricorn and Marcus data sets.